2014

High quality three-dimensional (3D) shape measurement using intensity-optimized dithering technique

Beiwen Li
Iowa State University

Recommended Citation

Li, Beiwen, "High quality three-dimensional (3D) shape measurement using intensity-optimized dithering technique" (2014). *Graduate Theses and Dissertations*. 13678.
https://lib.dr.iastate.edu/etd/13678

High quality three-dimensional (3D) shape measurement using intensity-optimized dithering technique

by

Beiwen Li

A thesis submitted to the graduate faculty
in partial fulfillment of the requirements for the degree of
MASTER OF SCIENCE

Major: Mechanical Engineering

Program of Study Committee:
Song Zhang, Major Professor
James H Oliver
Yan-Bin Jia

Iowa State University
Ames, Iowa
2014

TABLE OF CONTENTS

LIST OF FIGURES

ACKNOWLEDGEMENTS

I would like to take this opportunity to express my greatest gratitude to everyone who has helped me throughout my research. First and foremost, Dr. Song Zhang for giving me the privilege of joining this innovative and productive research group. His valuable instructions and insights have made me become a better researcher in this field of research.

Moreover, I would like to thank my committee members for their willingness and help in serving on my committee: Dr. James H. Oliver and Dr. Yan-Bin Jia. Dr. Oliver gave me a lot of senses of inspiration when I took his two classes and made me feel powerful after finishing the class projects. Dr. Jia has broadened my vision and enriched my knowledge of computer-science-related mathematics. Both of them helped me a lot in finishing this thesis and gave me some suggestions on how to better illustrate my research results.

Next, I would also like to thank my kind and supportive group members: Laura Ekstrand, William Lohry, Chen Gong, and Tyler Bell. Without their help and support in research and in daily life, I would never have an enjoyable experience of research and achieve satisfying results.

Last but not least, many thanks to my family members. Without their love and encouragement, I would never have had the opportunity to start my graduate study here and finish this research.

ABSTRACT

In past decades, there has been an upsurge in the development of three-dimensional (3D) shape measurement and its applications. Over the years, there are a variety of technologies developed including laser scanning, stereo vision, and structured light. Among these technologies, the structured-light technique has the advantages of fast computation speeds and high measurement resolution. Therefore, it has been extensively studied in this field of research. Nowadays, with the rapid development of digital devices, different kinds of patterns can be easily generated by a video projector. As a result, digital fringe projection (DFP), a variation of the structured light method, has had many applications owing to its speed and accuracy.

Typically, for a DFP system, ideal sinusoidal fringe pattern projection is required for high accuracy 3D information retrieval. Since traditional DFP projects 8-bit sinusoidal fringe patterns, it suffers from some major limitations such as the speed limit (e.g., 120 Hz), the requirement for nonlinear gamma calibration, and the rigid synchronization requirement between the projector and the camera. To overcome these limitations, the binary defocusing technology was developed which projects 1-bit square binary pattern and generates ideal sinusoidal pattern through projector defocusing.

In the past few years, the binary defocusing technique has shown great potential for many applications owing to its speed breakthroughs, nonlinear gamma calibration free and no rigid synchronization requirement between the camera and the projector. However, a typical square binary pattern suffers from some major limitations: (1) high-order harmonics, introduced by a square wave, which affect the accuracy of measurement, cannot be completely eliminated by projector defocusing; (2) a reduced measurement

volume since the projector needs to be properly defocused to generate the desired high-quality sinusoidal patterns; and (3) difficulty achieving high-quality measurements with wider square binary patterns.

The binary dithering technique, originally developed for printing technology, is found to have great potential for overcoming these aforementioned limitations of the square binary method. However, the binary dithering technique, which simply applies a matrix operation to the whole image, still has great room for improvement especially when the fringe patterns are not sufficiently defocused. Although there have been past efforts made to improve the performance of dithering techniques for 3D shape measurement, those approaches are either computationally expensive or fail to improve the quality with different amounts of defocusing.

In this research, we aim at further improving the binary dithering technique by optimizing the dithered patterns in intensity domain. We have developed both global and local optimization frameworks for improving dithered patterns. Our simulation and experimental results have demonstrated that: the global optimization framework improves the Bayer-order dithering technique by approximately 25% overall and up to 50% for narrower fringe patterns (e.g. fringe period of $T = 18$ pixels); the local optimization framework can improve the performance of a more advanced error-diffusion dithering technique by 20% overall and up to 40% for narrower fringe patterns (e.g. $T = 18$ pixels). Moreover, since the local algorithm involves optimizing a small image block and building up the desired-size patterns using symmetry and periodicity, it is much faster in terms of optimization time than the global algorithm.

CHAPTER 1. GENERAL INTRODUCTION

This chapter serves as a general introduction to the entire thesis. In this chapter, the relevant 3D shape measurement technologies will be introduced, the motivation and objectives will be presented, and the organization of the thesis will be explained. Part of this chapter was originally published in *Optics and Lasers in Engineering* (Dai et al., 2014b).

1.1 State of The Art

1.1.1 3D shape measurement techniques

This section introduces some major 3D shape measurement techniques that are closely related to this research. For each technique, the strengths and weaknesses will be addressed.

1.1.1.1 Laser scanning

3D laser scanning technology is widely adopted in 3D optical metrology. There are a variety of 3D scanners developed which can be divided into two major categories: time-of-flight (TOF) 3D laser scanners which requires no triangulation and triangulation-based 3D laser scanners.

(1) TOF laser scanner

The TOF laser scanner essentially emits pulses of laser light onto the object, and a laser range finder is used to detect the reflected pulse of light. The distance to a surface is calculated based on the round-trip traveling time of the emitted light pulse. Suppose the speed of light, c, and the round-trip time, t, are known; the distance is equal to $c \cdot t/2$. However, due to the extremely fast speed of the light, it is difficult to achieve a high depth resolution (e.g. a timing sensor resolution of 3.3 piscoseconds is required to resolve 1.00 mm in depth). Therefore, the majority of TOF technologies modulate the light source at a constant frequency and measure the phase difference before and after the round trip, and the depth is then determined from the phase difference, which is proportional to the depth.

The main advantage of the TOF laser scanner is its compact design, since the light source and the sensor have the same viewing angle. However, the TOF laser scanners usually have a limited spatial and depth resolution. This is owing to the complexity of manufacturing a sensor that can simultaneously record the light intensity and the phase information.

(2) Triangulation-based 3D laser scanner

The triangulation-based 3D laser scanner typically includes a laser emitter, a detector, and a lens which focuses the laser beam onto the detector. The laser light source shines a laser line or dot onto the object, and the reflected light will be sensed by the detector. The depth information can be retrieved by triangulating the laser emitting point, the reflecting point on the object surface, and the sensing point on the detector.

A triangulation-based laser scanner can achieve high spatial and depth resolution and is capable of measuring large scale objects, such as buildings or ships. However, the laser triangulation method is usually quite slow since only a laser line or dot is swept at a time, thus making it difficult to measure a rapidly moving object. Area-based 3D shape measurement can achieve faster measurement speeds and will be introduced next.

1.1.1.2 Stereo vision

The basic principle of a stereo vision system essentially imitates the human vision system: two cameras capture 2D images of 3D real world objects from two different viewing angles. The relationship between the real world 3D points and their perspective projections on 2D camera image planes is called epipolar geometry. Figure 1.1 illustrates the principle of a typical stereo vision system, where O_L and O_R are the centers of projection of the two cameras, E_L and E_R are the epipolar points, and P_L and P_R are the projections of the real world point P on the camera image planes. The projection line $\overline{PO_L}$ is viewed as a single point P_L on the left camera, while it is perceived as an epipolar line $\overline{E_R P_R}$ on the right camera. Similarly, the projection line $\overline{PO_R}$ will be seen as an epipolar line $\overline{E_L P_L}$ on the left camera.

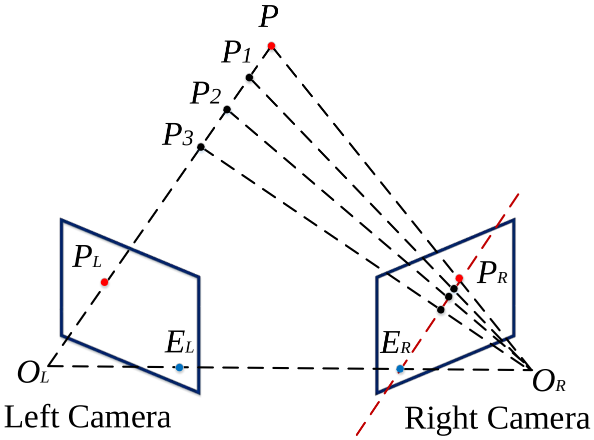

Figure 1.1 Schematic diagram of a stereo vision system.

The projection from a 3D world coordinate to a camera image coordinate is typically described by

$$s \begin{bmatrix} u \\ v \\ 1 \end{bmatrix} = A \begin{bmatrix} R & t \end{bmatrix} \begin{bmatrix} X \\ Y \\ Z \\ 1 \end{bmatrix}, \tag{1.1}$$

where $[X, Y, Z, 1]^T$ represents the point in the homogeneous world coordinate system,

$[u, v, 1]^T$ denotes the point in the homogeneous image coordinate system with the principle point $[u_0, v_0, 1]^T$, and A is the intrinsic matrix represented as

$$A = \begin{bmatrix} f_u & \alpha & u_0 \\ 0 & f_v & v_0 \\ 0 & 0 & 1 \end{bmatrix}. \tag{1.2}$$

Here, f_u and f_v are the focal lengths along u and v axes, respectively. $[R, t]$ is the extrinsic matrix that transforms the world coordinate to a camera lens coordinate, and s is the scale factor. Both the intrinsic and the extrinsic matrices can be determined through numerous camera calibration approaches (Duane, 1971; Sobel, 1974; Tsai, 1987; Zhang, 2000; Lavest et al., 1998; Albarelli et al., 2009; Strobl and Hirzinger, 2011; Huang et al., 2013b; Schmalz et al., 2011; Huang et al., 2013a).

The key point for a stereo vision system is to detect feature points and determine correspondence between two camera images. For each correspondence pair, the 3D point (X, Y, Z) can be uniquely determined in the least square sense by solving the over-determined system of linear equations: Eq. 1.1 for both cameras resulting in six equations and five unknowns. The stereo vision system has the merits of low cost and simple setup, and it also enables the measurement of a whole area at once, meaning it can achieve higher measurement speeds than laser scanning techniques. However, the stereo vision technique has the major difficulty that it is computationally expensive to find correspondence pairs. Moreover, in cases such as the existence of regions of uniform or periodical texture, the correspondence detection might fail.

1.1.1.3 Structured light

The basic principle of a structured-light system is similar to that of a stereo vision system, except that one of the two cameras is replaced with a projection device. The projection unit projects a known pattern onto the object to assist in the establishment of correspondence. Several different pattern coding strategies have been developed for structured-light systems, including random or pseudo-random codifications, and binary structured codifications and N-ary codifications.

(1) Random or pseudo-random codifications

In order to obtain the 3D information, the correspondence between a camera pixel and a projector pixel needs to be established, and this could be done by projecting digital pseudo-random patterns or using laser speckles (Huang et al., 2013c). In this way, the pixels are unique in both the u and v directions over the entire image. This method makes it easy to find correspondence pairs, and thus it is adopted in some applications, such as the first generation of Microsoft Kinect. However, the spatial resolution of this approach is limited by both the camera and projector spatial resolutions. Moreover, to determine 3D coordinates, two sets of Eq. 1.1 are needed which contain six linear equations but only five unknowns (X, Y, Z, s_p, s_c), where s_p and s_c are the scale factors of the projection unit and camera respectively. Owing to the redundancy of one additional equation, the encoded pattern does not have to be unique in both the u and v directions, and thus it is natural to choose patterns that vary in only one direction. One of the popular approaches of this type is binary structured codification.

(2) Binary structured codifications

Binary structured codifications essentially project a sequence of binary coded patterns, as illustrated in Fig. 1.2, onto the object, to define codewords. Then the 3D information is decoded by referring to the codeword of each point (Posdamer and Altschuler, 1982). This approach is robust to noise since only two intensity levels (0s and 255s) are used. However, the resolution of this method is determined by the narrowest binary pattern used shown in Fig. 1.2(a), the length of a black or white stripe is usually bigger than a projector pixel, thus making it difficult to reach projector pixel-level spatial resolution. In addition, for high-resolution measurement, it requires projection of many patterns (e.g. more than 10 images to encode 1024 columns or 768 rows); therefore, it is difficult to achieve high-speed measurement. To address this problem, N-ary codifications could be used which use more than two grayscale values.

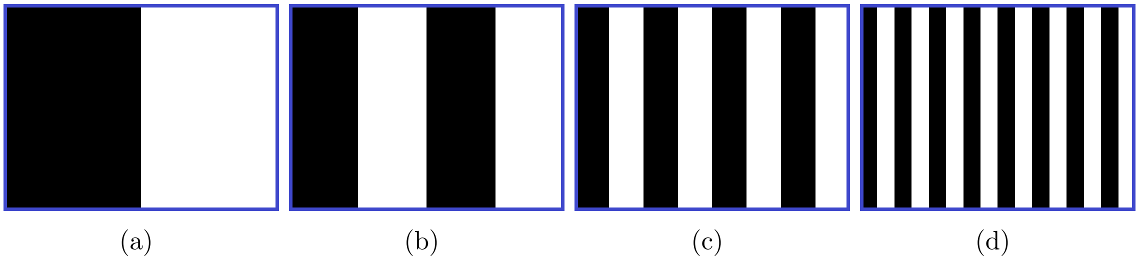

(a) (b) (c) (d)

Figure 1.2 Example of codified binary pattern sequence

(3) N-ary codifications

Instead of using only two intensity levels (0 and 255), N-ary codifications divide the full range of grayscale values (0 to 255) into N bins, and the codeword for each pixel is determined by the intensity ratio (Carrihill and Hummel, 1985; Chazan and Kiryati, 1995). N-ary codifications overcome the speed limitation of the binary structured codifications by reducing the number of patterns for projection. However, compared with binary structured codifications, N-ary codifications are more sensitive to noise and image defocusing due to the increased range of grayscale values. Furthermore, similar to the other two aforementioned codifications, they are still limited by the projector pixel resolution. To overcome the limitations of this coding strategy, several other approaches using phase-shifting techniques have been developed, including the triangular method (Jia et al., 2007) and the trapezoidal method (Huang et al., 2005). These approaches could reach camera pixel-level accuracy and are less sensitive to image defocusing. However, the problem caused by defocusing cannot be completely circumvented.

1.1.1.4 Digital fringe projection (DFP)

According to Zhang (2010), the above mentioned 1-dimensional varying (binary, N-ary, triangular, trapezoidal) patterns eventually become a sinusoidal shape if properly defocused. Thus, it is natural to think of using sinusoidal patterns. Sinusoidal patterns have the potential to reach camera pixel-level accuracy since for each cross-section, the intensity values vary from one point to another and this variation is differentiable between neighboring pixels. DFP is a technology that uses a digital video projector to project computer-generated sinusoidal fringe patterns onto an object; from the distorted fringe image captured by the camera, the 3D information can be retrieved. Unlike the intensity-based methods, the phase information is used in DFP technology to retrieve the 3D information since phase information is more robust to noise. A detailed description of 3D reconstruction using phase information will be introduced in Chapter 2.

In recent years, DFP technology has been extensively adopted because of its speed and accuracy (Geng, 2011). However, DFP technology is not trouble free. Since it requires the projection of 8-bit sinusoidal patterns, the measurement speed is limited by the maximum frame rate of the projector (typically 120 Hz) (Zhang, 2010). Moreover, it requires precise camera-projector synchronization (Lei and Zhang, 2010). Furthermore, most video projectors are nonlinear, making it difficult to generate high quality phase without gamma correction (Lei and Zhang, 2009).

1.1.2 Digital fringe projection technology using binary defocusing technique

To address the challenges of the conventional DFP technique, our research group recently developed the binary defocusing technique (Lei and Zhang, 2009), which generates sinusoidal fringe patterns by projecting 1-bit square binary patterns with an out-of-focus projector. This technique has successfully made speed breakthroughs (Zhang et al., 2010). Meanwhile, it is gamma calibration free and does not require rigid camera-projector synchronization. However, the binary defocusing technique is not trouble free: the measurement accuracy is affected by high-order harmonics, and the measurement range is smaller than that for the conventional DFP technique (Xu et al., 2011).

Modulation techniques were proposed to improve the fringe quality of the binary defocusing technique; these modulate the binary patterns according to the ideal sinusoidal patterns. These techniques include 1D modulations and 2D modulations. The pulse width modulation (PWM) techniques (Ayubi et al., 2010; Wang and Zhang, 2010; Zuo et al., 2012, 2013) belong to the 1D modulation category. The PWM technique essentially modulates the binary pattern such that the high-frequency harmonics can be more easily suppressed or eliminated after defocusing. The 1D methods all achieved better measurement quality when compared with the squared binary method. However, these techniques have limited improvements when fringe stripes are wide (Wang and Zhang, 2012). Xian and Su (2001) proposed a 2D area modulation technique that could generate high-quality fringe patterns if the manufacturing precision is high enough. But this area modulation technique is difficult to implement in a DFP system since it requires more precisely manufactured pixels than a digital video projector can provide. Our research group recently proposed another 2D modulation method (Lohry and Zhang, 2012) that locally modulates the pixels so that it is easier to generate an ideal sinusoidal pattern by defocusing the modulated pattern. However, it is not suited for the wide fringe patterns (Lohry and Zhang, 2013).

Dithering, also called halftoning, has been extensively studied in the fields of image processing and printing (Schuchman, 1964). Various dithering techniques have been proposed over the years including random dithering (Purgathofer et al., 1994), ordered dithering (Bayer, 1973), and error-diffusion dithering (Kite et al., 2000). Wang and Zhang (2002) have demonstrated that the Bayer dithering method could substantially improve the measurement quality even when the fringe stripes are very wide. However, if the patterns are nearly focused, the residual error becomes ineligible.

Recently, Dai and Zhang (2013) proposed a phase-based optimization framework to optimize the Bayer-ordered dithering technique when the projector is nearly focused. This method performs optimization in the phase domain by iteratively mutating the status (0 or 1) of a binary pixel. It was demonstrated that for both narrow and wide fringe stripes, substantial improvements could be achieved. However, this method was not very stable for different amounts of defocusing.

1.2 Motivation And Objectives

As discussed in the previous section, the binary dithering technique could substantially improve the measurement quality of the binary defocusing technique. However, there is still room for improvement since it only applies matrices to the whole image. The existing optimization framework has demonstrated its success in improving the binary dithering technique. However, it suffers from non-stable performance over different amounts of defocusing. Therefore, developing new optimization approaches for the binary dithering technique is necessary to address this limitation.

In this research, we aim at developing new algorithms that could further improve the binary dithering technique and simultaneously achieving a more consistent accuracy over different amounts of defocusing. Instead of optimizing the dithered patterns in the phase domain (Dai and Zhang, 2013), we propose both a global and a local optimization framework that optimize the dithered patterns in the intensity domain. In this thesis, we will introduce the related theoretical background and the basic principles of these optimization methods. Moreover, simulations and experimental results will be shown to verify their performance.

1.3 Thesis Organization

This thesis is organized as follows: Chapter 2 introduces the basic principles of the DFP technique that we used for 3D shape measurement. Chapter 3 discusses the theoretical background of the binary defocusing technique and subsequent improvements. Chapter 4 illustrates our optimization framework, and Chapter 5 summarizes the whole thesis and discusses some directions for future work.

CHAPTER 2. DIGITAL FRINGE PROJECTION AND 3D RECONSTRUCTION

In this chapter, some fundamentals of digital fringe projection which were adopted in this research will be introduced. Meanwhile, the 3D reconstruction frameworks will also be illustrated, which includes the phase-shifting algorithms and phase-to-height conversion. Part of this chapter was originally published in *SPIE proceedings* (Dai et al., 2013).

2.1 Digital Fringe Projection (DFP) System

Figure 2.1 shows the typical setup of a DFP system. A computer generated known fringe pattern will be sent to the video projector and projected onto the object to be measured. Then, a camera is used to capture the distorted fringe image and send it to the computer for further analysis. Finally, the computer will analyze the captured fringe image and preform a 3D reconstruction based on the distortion of fringe pattern. Typically, a sinusoidal pattern will be used for projection, as shown in Fig. 2.1, each vertical line corresponds to a unique phase value in the frequency domain. Here we use phase value for 3D reconstruction since compared with intensity value, phase value is not sensitive to the ambient light variations (Karpinsky and Zhang, 2012).

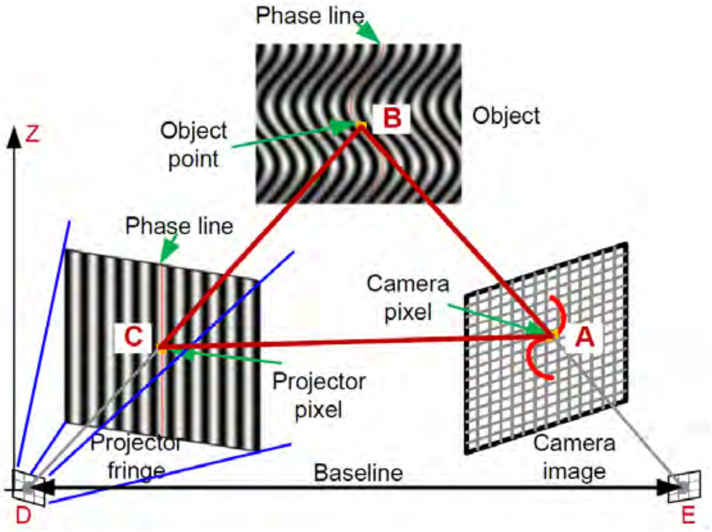

Figure 2.1 Typical setup of a DFP system.

2.2 Phase-Shifting Algorithms

In this research, phase-shifting algorithms are used for phase extraction, which are widely applied in optical metrology due to their speed and accuracy (Malacara, 2007). Theoretically, a fringe image $I(x, y)$ could be expressed as

$$I(x, y) = I'(x, y) + I''(x, y) \cos[\phi(x, y) + \delta], \tag{2.1}$$

where $I'(x, y)$ is the average intensity, $I''(x, y)$ the intensity modulation, δ is the phase-shift, and $\phi(x, y)$ the phase to be solved for. Since there are three unknowns $I'(x, y)$, $I''(x, y)$ and $\phi(x, y)$ in this equation, therefore, at least three different phase-shifted images are needed for extracting the phase $\phi(x, y)$.

In this section, some different phase-shifting algorithms will be introduced, which includes three-step phase-shifting that requires the least images and also N-step phase shifting which solves a more general case. Finally, a multi-frequency phase-shifting algorithm will be introduced for absolute phase retrieval.

2.2.1 Three-step phase-shifting algorithm

For a three-step phase-shifting algorithm, three fringe images with equal phase shifts of $2\pi/3$ are used, which could be described as

$$I_1(x,y) = I'(x,y) + I''(x,y)\cos(\phi - 2\pi/3), \tag{2.2}$$

$$I_2(x,y) = I'(x,y) + I''(x,y)\cos(\phi), \tag{2.3}$$

$$I_3(x,y) = I'(x,y) + I''(x,y)\cos(\phi + 2\pi/3). \tag{2.4}$$

Then, by simultaneously solving the three equations, the phase $\phi(x,y)$ could be obtained as

$$\phi(x,y) = \tan^{-1}\frac{\sqrt{3}(I_1 - I_3)}{2I_2 - I_1 - I_3}. \tag{2.5}$$

2.2.2 N-step phase-shifting algorithm

Although three equally phase-shifted fringe images are enough for phase extraction, however, the accuracy of the phase obtained from three-step is limited. Typically, the more steps used, the better the measurement quality which could be achieved. More generally, for an N-step phase-shifting algorithm with equal phase shifts, the fringe images can be described as

$$I_k(x,y) = I'(x,y) + I''(x,y)\cos(\phi + 2k\pi/N). \tag{2.6}$$

In this case, the phase $\phi(x,y)$ could be solved by the following equation:

$$\phi(x,y) = \tan^{-1}\left[\frac{\sum_{k=1}^{N} I_k \sin(2k\pi/N)}{\sum_{k=1}^{N} I_k \cos(2k\pi/N)}\right]. \tag{2.7}$$

However, the phase provided by phase-shifting algorithms are wrapped phase or relative phase ranging $[-\pi, +\pi)$ with 2π discontinuities. A continuous phase map can be obtained by adopting a spatial (Ghiglia and Pritt, 1998) or temporal phase unwrapping algorithm (Wang and Zhang, 2011). In this research, we adopted a multi-frequency phase-shifting algorithm (Wang and Zhang, 2011) for absolute phase retrieval which will be introduced in the next subsection.

2.2.3 Multi-frequency phase-shifting algorithm

As mentioned previously, the phase obtained from a single fringe frequency using phase-shifting algorithm is wrapped with 2π discontinuities. To obtain the absolute phase map, we can take advantage of the wrapped phase extracted using different fringe frequencies, which is called multi-frequency phase-shifting algorithm.

Taking the two-frequency phase-shifting algorithm as an example, its basic principle could be illustrated as follows. Theoretically, the absolute phase $\mathbf{\Phi}$ could be represented by spatial distance $h(x,y)$ and fringe period T,

$$\mathbf{\Phi} = 2\pi \frac{C \cdot h(x,y)}{T}, \tag{2.8}$$

where C is a system constant. As a result, for the absolute phase $\mathbf{\Phi}_1$ and $\mathbf{\Phi}_2$ with different fringe period, their difference $\Delta\mathbf{\Phi}_{12}$ could be deduced as

$$\Delta\mathbf{\Phi}_{12} = \mathbf{\Phi}_1 - \mathbf{\Phi}_2 = 2\pi \frac{C \cdot h(x,y)}{T_{12}^{eq}}, \tag{2.9}$$

where $T_{12}^{eq} = T_1 T_2 / |T_1 - T_2|$ is the equivalent fringe period between T_1 and T_2. From the N-step phase-shifting algorithm introduced in Sec. 2.2, we have already obtained the wrapped or relative phase ϕ_1 and ϕ_2 with 2π discontinuities. The relationship between the absolute phase and the relative phase could be expressed as

$$\phi = \mod(\mathbf{\Phi}, 2\pi). \tag{2.10}$$

Here, mod is a modulus operator. Therefore, the difference $\Delta\phi_{12}$ between the two relative phase ϕ_1 and ϕ_2 could be represented as

$$\Delta\phi_{12} = \mod(\mathbf{\Phi}_1 - \mathbf{\Phi}_2, 2\pi) = \mod\left[2\pi \frac{C \cdot h(x,y)}{T_{12}^{eq}}, 2\pi\right]. \tag{2.11}$$

In this case, if the equivalent fringe period T_{12}^{eq} is properly chosen in a way such that $C \cdot h(x,y)/T_{12}^{eq} < 1$, then a continuous phase map could be obtained without 2π discontinuities.

However, practically the two-frequency algorithm is not enough since it is very sensitive to the noise. Therefore, in practice, at least three frequencies are utilized to retrieve the absolute phase. Consider we have another set of fringe patterns with fringe period T_3 and extracted relative phase ϕ_3, then the difference $\Delta\phi_{123}$ between the two relative phase ϕ_{12} and ϕ_3 could be obtained as

$$\Delta\phi_{123} = \mod(\mathbf{\Phi}_{12} - \mathbf{\Phi}_3, 2\pi) = \mod\left[2\pi\frac{C \cdot h(x,y)}{T^{eq}_{123}}, 2\pi\right]. \tag{2.12}$$

Here T^{eq}_{123} is the equivalent fringe period obtained by $T^{eq}_{123} = T_{12}T_3/\left|T_{12} - T_3\right|$. Similarly, if we let $C \cdot h(x,y)/T^{eq}_{123} < 1$, then the absolute phase map could be obtained. Once this absolute phase map is retried, then by reversely unwrapping the phase, we can obtain the absolute phase map of the shortest fringe period. It should be noted that the phase of the shortest fringe period is usually desirable since it better preserves the detailed information of the measured object and provides better accuracy.

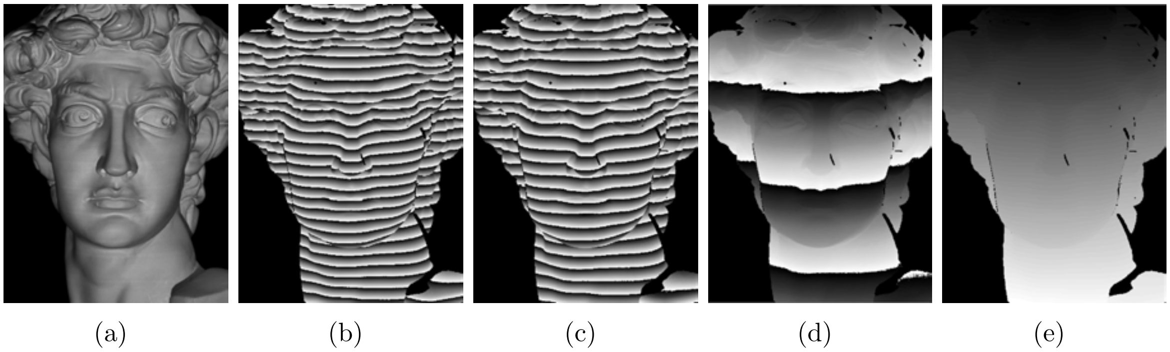
(a) (b) (c) (d) (e)

Figure 2.2 Absolute phase retrieval using three-frequency phase-shifting algorithm. (a) Picture of the sculpture; (b) wrapped phase map obtained from patterns with fringe period $T_1 = 18$ pixels; (c) wrapped phase map obtained from patterns with fringe period $T_2 = 21$ pixels; (d) wrapped phase map obtained from patterns with fringe period $T_3 = 159$ pixels; (e) absolute phase map obtained by applying three-frequency phase-shifting algorithm.

Figure 2.2 illustrates a typical three-frequency phase-shifting algorithm that we adopted for absolute phase retrieval, which includes the relative phase maps obtained from high-frequency ($T = 18$), medium-frequency ($T = 21$) and low-frequency ($T = 154$) fringe patterns as well as the absolute phase map obtained after applying this algorithm. It demonstrates that this algorithm can indeed succeed in retrieving the absolute phase map using the fringe images of different frequencies.

2.3 Phase-To-Depth Conversion

Once the absolute phase is obtained, the next step is to determine the depth z of the measured object. In this research, a reference-plane-based approach introduced by Zhang et al. (2002) is used for phase-to-depth conversion. Its schematic diagram is shown in Fig. 2.3. Basically, a reference plane is first measured as a reference of subsequent measurements, the depth of the object is then measured relative to that.

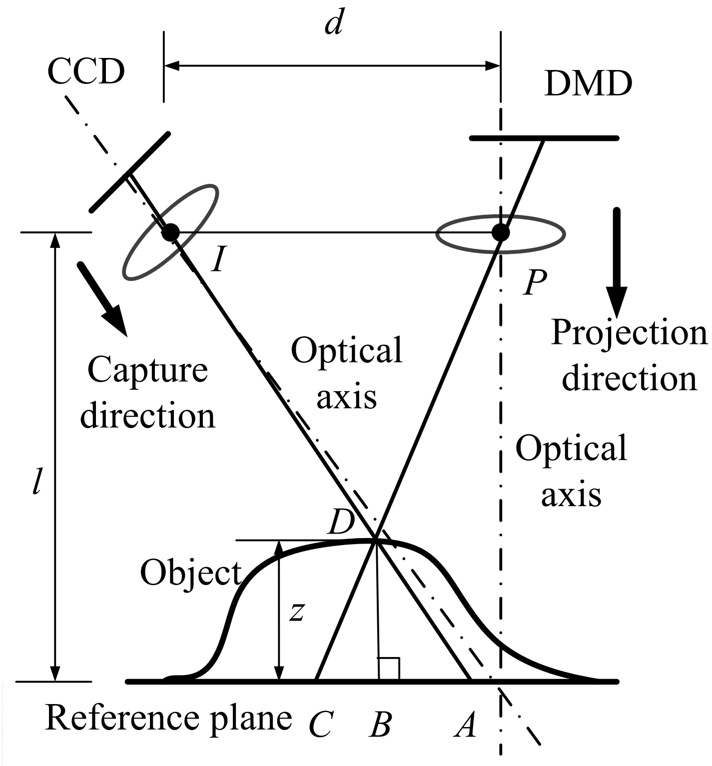

Figure 2.3 Schematic diagram of phase-to-height conversion.

According to the geometry of the system, the depth z could be represented as

$$z(x,y) = \overline{DB} = \frac{\overline{AC} \cdot l}{d \cdot (1 + \frac{\overline{AC}}{d})} \approx \frac{l}{d}\overline{AC} \propto \mathbf{\Phi}_A - \mathbf{\Phi}_C, \tag{2.13}$$

where $\mathbf{\Phi}_A$ and $\mathbf{\Phi}_C$ are the absolute phase values at points A and C respectively. From the projector point of view, point D and point C share the same phase value, which means $\mathbf{\Phi}_D = \mathbf{\Phi}_C$. In this case, it can be deduced that

$$z(x,y) \propto \mathbf{\Phi}_A - \mathbf{\Phi}_D = \mathbf{\Phi}^o(x,y) - \mathbf{\Phi}^r(x,y), \tag{2.14}$$

where $\mathbf{\Phi}^o$ and $\mathbf{\Phi}^r$ are the absolute phase map of the object and the reference plane respectively. Assume that the reference plane has a depth value of z_0, then the depth of the measured point on the object can be represented as (Xu et al., 2011)

$$z(x,y) = z_0 + c \times [\mathbf{\Phi}^o(x,y) - \mathbf{\Phi}^r(x,y)], \tag{2.15}$$

where c is a system constant and can be obtained through calibration.

2.4 Summary

In this chapter, the basic idea of DFP system is discussed. Then the phase-shifting algorithm for phase extraction is introduced, and finally the 3D reconstruction based on phase-to-depth conversion is also illustrated. In the next chapter, we will be introducing the implementation of the binary defocusing technique which further extends the speed and flexibility of a DFP system.

CHAPTER 3. BINARY DEFOCUSING TECHNIQUES

In previous chapter, some fundamentals about the DFP technique and the 3D reconstruction framework were introduced. In this chapter, we will explain the binary defocusing techniques, which make the DFP method more flexible and break the speed bottleneck of conventional DFP techniques. First of all, some fundamentals of DLP technology will be introduced which both motivate and provide the foundation of the development of binary defocusing techniques. Then, the principles of the binary defocusing technique will be explained. Finally, the binary dithering techniques will be introduced which greatly improve the performance of the squared binary defocusing technique. Part of this chapter was originally published in the *SPIE proceedings* (Li et al., 2013) and *Optics and Lasers in Engineering* (Li et al., 2014).

3.1 Fundamentals of Digital-Light-Processing (DLP) Technology

Digital-Light-Processing (DLP) technology is based on an optical semiconductor called the digital micro-mirror device (DMD). This very precise light switch modulates the light digitally with an array of digital micro-mirrors which correspond to the pixels in the projected image. When a digital graphics signal enters the DLP system, the micro-mirrors will be tilted either toward or away from the light source by a tiny electrode beneath each DMD cell. The working principle of the DMD is illustrated in Fig. 3.1. The digital graphics signal will force the mirror to switch on ($+\theta_L$) or off ($-\theta_L$). A

DLP projector produces grayscale values by time integration (Hornbeck, 1997), which means that the brightness of a pixel will be controlled by the portion of the time that its corresponding micro-mirror is switched on. For example, if the mirror is switched on 100% of the time, then a grayscale value of 255 will be produced. On the other hand, if the mirror is always switched off, then a grayscale value of 0 will be created.

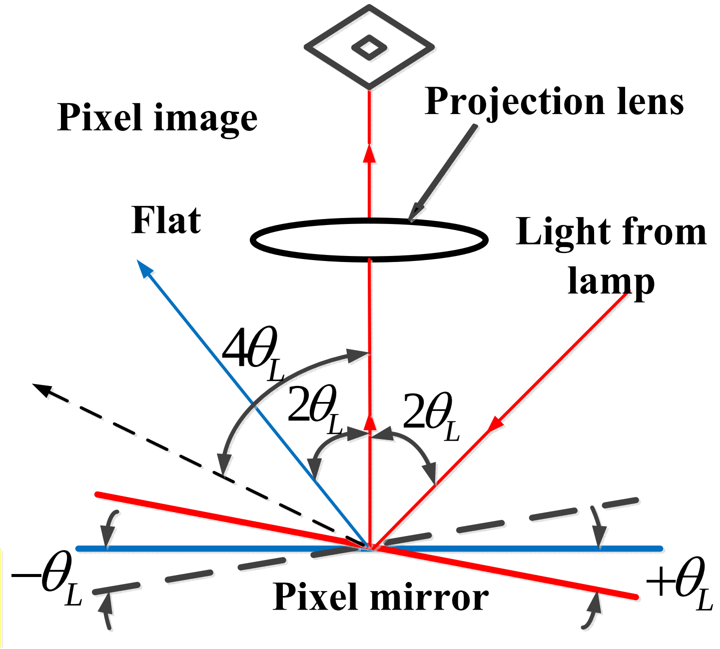

Figure 3.1 Optical switching mechanism of digital micromirror device (DMD)

In order to better examine the working principle of DLP, a simple test was carried out for our inexpensive DLP projector (Dell M109S). A photodiode sensor (Thorlabs FDS100) was used to detect the output light and the photoelectric current signal was converted into voltage signal and monitored by an oscilloscope. Figure 3.2 shows the result when uniform images are applied to the projector. In order to simplify the test, only the green channel is used. These experimental results showed that when the DLP projector is fed with a pure green image (RGB = (0, 255, 0)), the channel is filled by almost 100%. When the grayscale value is reduced to 128 and 64 respectively, it generates irregular output, and the portion of the channel filled is reduced. In this case, if a sinusoidal fringe pattern with grayscales varying from 0 to 255 is supplied, we would need to capture the whole projection cycle in order to obtain a correct capture of the projected image. For high-speed measurement, however, this is undesirable since the camera exposure time usually needs to be very short (Gong and Zhang, 2010).

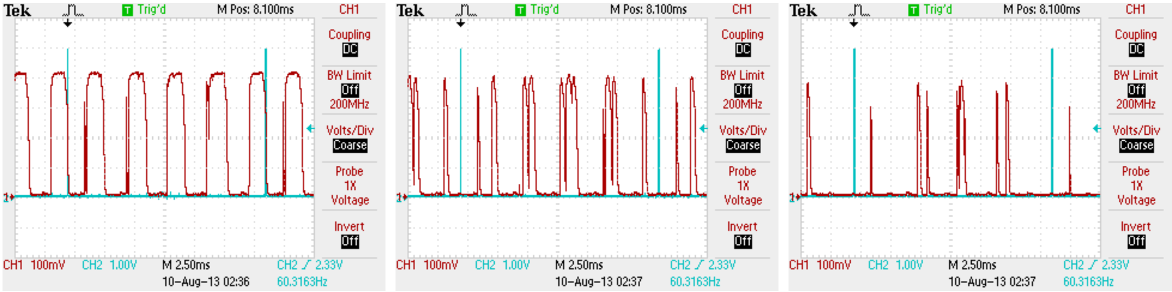

(a) (b) (c)

Figure 3.2 Example of the voltage output at the photodiode (in red) and projector refresh signal (in blue) if the DLP projector is fed with a uniform green image with different grayscale values. (a) Green = 255; (b) Green = 128; (c) Green = 64.

3.2 Binary Defocusing Technique

In the previous section, we have shown that if a DLP micro-mirror is fed with a grayscale value of 0 or 255, it will remain on or off within the whole projection cycle. Thus, if a DLP projector is fed with a binary image which only contains two grayscale values (0 or 255), we do not have to capture the whole projection cycle; this is beneficial for high-speed measurement. However, traditionally, 8-bit sinusoidal patterns are used for the DFP technique, requiring the capture of the full projection cycle. In order to overcome this limitation, we could approximate a sinusoidal fringe pattern by projecting a binary pattern with a properly defocused projector; this is called "binary defocusing technique."

Figure. 3.3 shows a schematic diagram comparing the traditional focused sinusoidal projection and the binary defocusing technique, illustrating these two approaches to generating a sinusoidal fringe pattern. Traditionally, the projector was directly fed with

8-bit sinusoidal patterns. With a focused projector, a sinusoidal pattern can be visualized on the screen. In contrast, the binary defocusing technique feeds the projector with 1-bit square binary patterns. If the projector is properly defocused, then a sinusoidal fringe pattern can be generated.

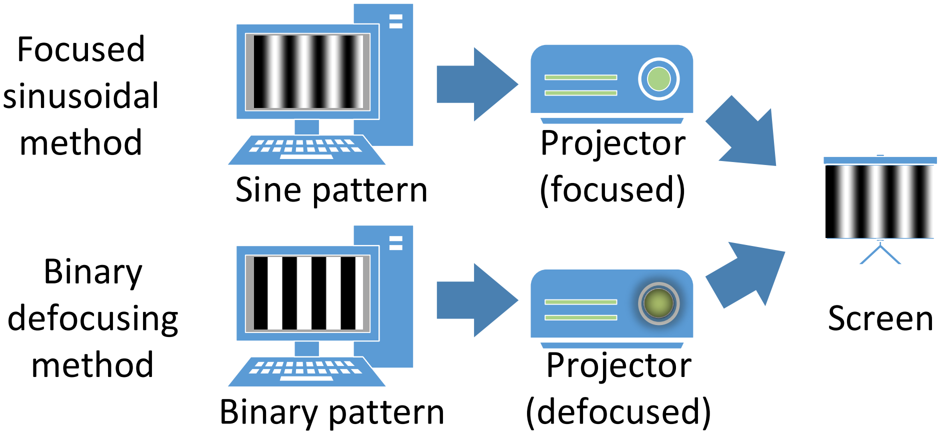

Figure 3.3 Schematic diagram comparing focused sinusoidal projection and the binary defocusing technique.

The theoretical background of binary defocusing is illustrated as follows. A binary pattern can be regarded as a square wave in mathematics. If we take a Fourier series expansion of the square wave, the first order harmonic represents the ideal sinusoidal wave, while higher order harmonics represent the detailed features of the square wave. It is important to note that the square wave only contains odd-order harmonics, which indicates that if a low pass filter that can eliminate or suppress higher order harmonics is applied, an ideal sinusoidal wave can be approximated. The projector defocusing technique creates a smoothing effect on the projected image which can be modeled as a Gaussian filter, meaning that if the projector is properly defocused to a certain degree, the projected binary image would be blurred such that a quasi-sinusoidal fringe pattern is generated (Lei and Zhang, 2009).

Figures 3.4(a) and 3.4(b) show the example of a squared binary pattern with a period of $T = 18$ pixels and its resultant pattern after Gaussian smoothing. Here, a Gaussian filter with the size of 13×13 and a standard deviation of $13/3$ is used in order to emulate the projector defocusing effect. Figure 3.4(c) shows the cross section of the defocused binary pattern and Fig. 3.4(d) shows the cross section of the phase error obtained in this case. Here, the phase was calculated using the three-step phase-shifting algorithm as introduced in Subsec. 2.2.1, and the phase error was evaluated by comparing this phase with the phase obtained using ideal sinusoidal patterns. This simulation indicates that if the pattern is properly blurred, a quasi-sinusoidal fringe pattern is indeed generated. Moreover, the phase error arising from this set of patterns is quite small with an root-mean-square (rms) error of 0.017 rad. It is important to note that for all simulations in this chapter, a zero-mean Gaussian noise with a standard deviation of 0.01 in intensity is added to the original patterns in order to emulate the noise in a real experiment.

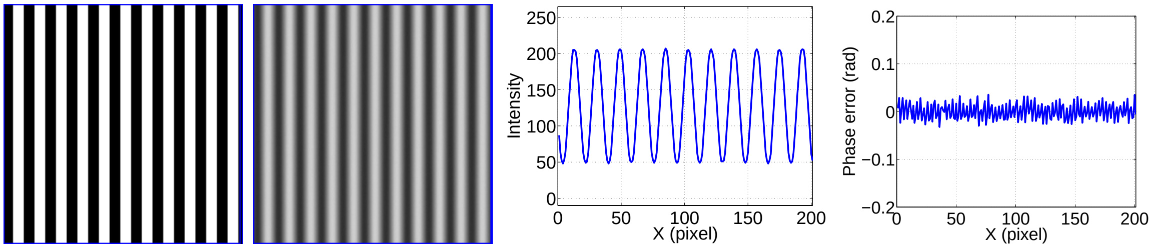

(a) (b) (c) (d)

Figure 3.4 Example that applying a Gaussian filter to a squared binary pattern can result in a quasi-sinusoidal pattern. (a) A squared binary pattern with a period $T = 18$ pixels; (b) the resultant pattern of (a) after Gaussian smoothing with a filter size of 13×13; (c) cross section of (b); (d) cross section of the phase error with rms error of 0.017 rad.

However, the binary defocusing technique is not trouble free. Since it requires the precise control of the projector defocusing level, either too focused or too defocused could cause problem. Figure 3.5 shows the simulation results when the pattern is too focused, from which we can see that a nearly focused square binary pattern cannot well represent a sinusoidal pattern, as is shown in Fig. 3.5(c). Figure 3.5(d) shows that the phase error arising from this set of patterns is quite large (rms error of 0.062 rad), which is almost three times worse than the previous case. Similarly, Figure 3.6 shows the simulation results when the pattern is too defocused. It illustrates that if the pattern is too defocused, the phase error is also very large [Fig. 3.6(d)], with an rms error of 0.068 rad. The reduced signal-to-noise ratio caused by over defocusing, as is shown in Fig. 3.6(c), should account for this phenomenon.

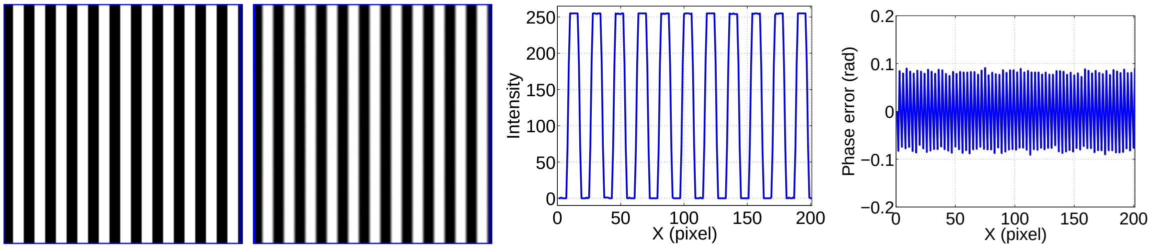

(a) (b) (c) (d)

Figure 3.5 Simulation of binary defocusing using nearly focused fringe patterns (fringe period $T = 18$ pixels). (a) Original pattern; (b) the resultant pattern of (a) after Gaussian smoothing with filter-size of 3×3; (c) cross section of (b); (d) cross section of the phase error with rms error of 0.062 rad.

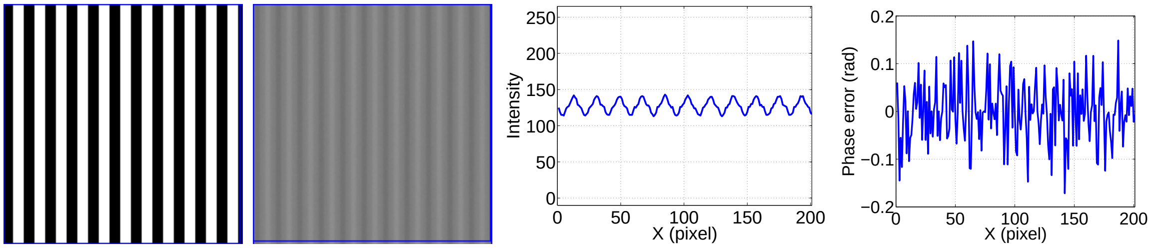

(a) (b) (c) (d)

Figure 3.6 Simulation of binary defocusing using over defocused fringe patterns (fringe period $T = 18$ pixels). (a) Original pattern; (b) the resultant pattern of (a) after Gaussian smoothing with filter-size of 21×21; (c) cross section of (b); (d) cross section of the phase error with rms error of 0.068 rad.

Furthermore, if the fringe period for the square binary pattern is very wide, it cannot well generate a sinusoidal pattern even with the same amount of defocusing (Gaussian filter size of 13×13). Figure 3.7 shows the simulation results when the binary defocusing technique is applied on a very wide fringe period of $T = 60$ pixels, from which we can see that even though the square binary pattern is properly defocused, it still cannot well represent a sinusoidal wave, as is shown in Fig. 3.7(c). Moreover, the phase error obtained using this set of patterns is even larger, as shown in Fig. 3.7(d), with an rms error of 0.150 rad. However, patterns with wide fringe periods are still useful especially when using a multi-frequency phase-shifting algorithm as introduced in Subsec. 2.2.3. Therefore, in order to improve the fringe quality, there are several techniques carried out to modulate the square binary fringe patterns. Among all these techniques, the binary dithering technique is found to be effective at addressing the limitations of the binary defocusing technique. In the next section, the principles of binary dithering techniques will be introduced.

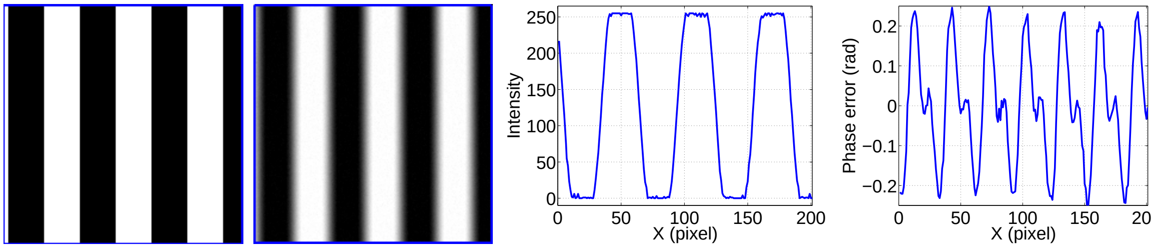

(a) (b) (c) (d)

Figure 3.7 Simulation of binary defocusing using wide fringe patterns ($T = 60$ pixels). (a) Original pattern; (b) the resultant pattern of (a) after Gaussian smoothing with filter-size of 13×13; (c) cross section of (b); (d) cross section of the phase error with rms error of 0.150 rad.

3.3 Binary Dithering Techniques

Binary dithering refers to a technique that renders the original image with only 1-bit color and meanwhile randomizes the quantization error (Wang and Zhang, 2002). Figure 3.8 illustrates the example of applying dithering techniques on a general grayscale image and then on a sinusoidal pattern. In this subsection, the three most extensively used dithering techniques will be introduced, which include the bayer-ordered dithering technique (Bayer, 1973), the Floyd and Steinberg (1976) error-diffusion dithering technique and the Stucki (1981) error-diffusion dithering technique.

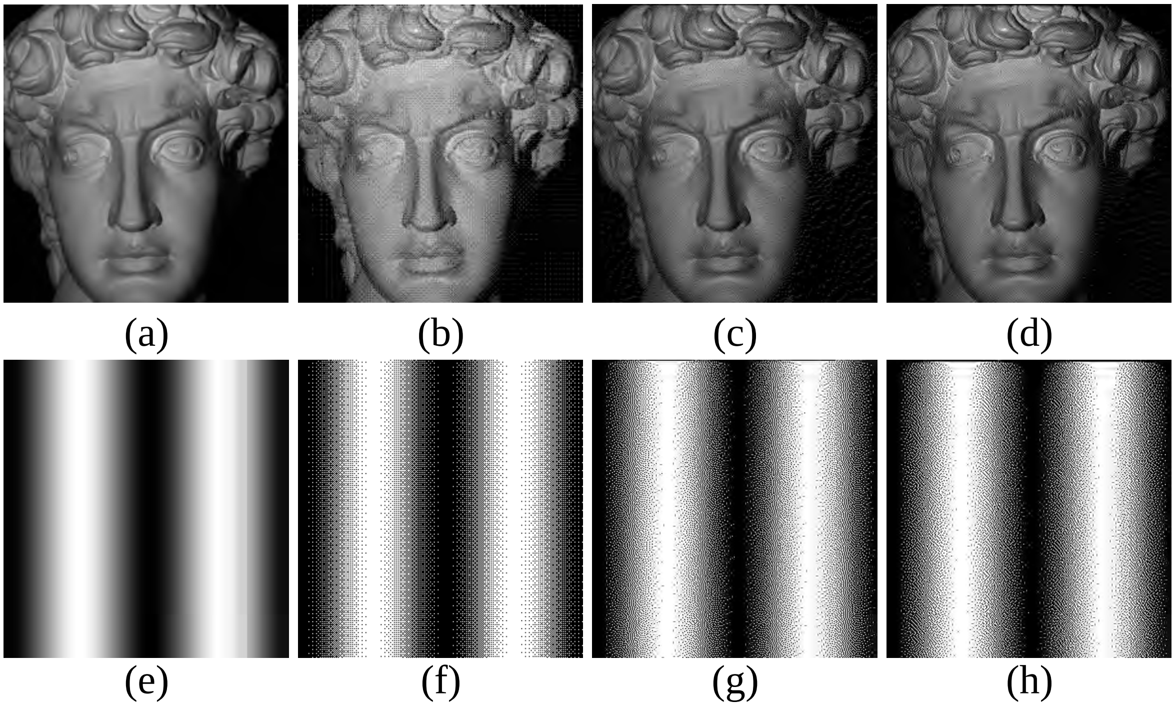

Figure 3.8 Illustration of dithering technique. (a) Original image of a general 8-bit grayscale image; (b) binary dithered image of (a) using Bayer-ordered dithering technique; (c) binary dithered image of (a) with the Floyd-Steinberg error-diffusion technique; (d) binary dithered image of (a) with the Stucki error-diffusion technique; (e) original image of a sinusoidal fringe pattern; (f) binary dithered image of (e) using Bayer-ordered dithering technique; (g) binary dithered image of (e) with the Floyd-Steinberg error-diffusion technique; (h) binary dithered image of (e) with the Stucki error-diffusion technique

The Bayer-ordered dithering technique, rather than using a simple threshold, compares the original image with a 2D grid of thresholds called the Bayer kernel, and then the original image is quantized according to the corresponding pixels in the Bayer kernel. Typically the threshold values in the dither pattern are different from one pixel to another, and thus the randomization of quantization error is achieved. According to Bayer (Bayer, 1973), an optimal dithered image with the noise being as high frequency as possible can be achieved if the size of the Bayer kernel is 2^N. Then the noise can be effectively reduced by a low-pass filter. The simplest Bayer dither pattern with a size of

2×2 can be obtained as follows

$$M_1 = \begin{bmatrix} 0 & 2 \\ 3 & 1 \end{bmatrix}, \tag{3.1}$$

Then, larger Bayer kernel can be obtained by

$$M_{n+1} = \begin{bmatrix} 4M_n & 4M_n + 2U_n \\ 4M_n + 3U_n & 4M_n + U_n \end{bmatrix}, \tag{3.2}$$

where U_n refers to an $n \times n$ unit matrix. After applying the Bayer kernel, the original image is then effectively quantized according to the threshold values in the Bayer kernel. For the binary defocusing technique, ideal sinusoidal patterns can be quantized by this Bayer-ordered dithering. It has been proven that Bayer-ordered dithering succeeds in providing valid results in 3D shape measurement (Wang and Zhang, 2002)

Error-diffusion techniques are more extensively employed since they can better represent the original image with the quantization errors propagation. For each error-diffusion technique, the pixels are quantized in a specific order such that the quantization error of the pixel in process is propagated forward to the local unprocessed pixels. Its basic principle can be described by the following equation

$$\tilde{f}(i,j) = f(i,j) + \sum_{k,l \in S} h(k,l)e(i-k, j-l). \tag{3.3}$$

Here, $f(i,j)$ refers to the pixel of the original image, and $\tilde{f}(i,j)$ stands for the modified input pixel. The modified input pixel $\tilde{f}(i,j)$ is then quantized and the output image is obtained. This equation explains how the quantization error $e(i,j) = f(i,j) - \tilde{f}(i,j)$ is propagated to the neighboring pixels by applying a 2D weighting function $h(i,j)$, which is known as a diffusion kernel. There are a variety of error-diffusion algorithms based on different selected diffusion kernels. Floyd-Steinberg error-diffusion and Stucki error-diffusion techniques are the two most extensively used error-diffusion techniques. The diffusion kernel of Floyd-Steinberg error-diffusion is written as

$$h(i,j) = \frac{1}{16}\begin{bmatrix} - & * & 7 \\ 3 & 5 & 1 \end{bmatrix}, \tag{3.4}$$

Here, $-$ refers to the previously processed pixel, $*$ represents the pixel in process. It is worth to note that the kernel elements should sum to one so that the local average of the image does not change. Similarly, the Stucki error-diffusion kernel is written as

$$h(i,j) = \frac{1}{42}\begin{bmatrix} - & - & * & 8 & 4 \\ 2 & 4 & 8 & 4 & 2 \\ 1 & 2 & 4 & 2 & 1 \end{bmatrix}. \tag{3.5}$$

In order to illustrate the enhancement that the binary dithering technique has on the binary defocusing technique, we did the exact same simulation for the binary dithered patterns as for the square binary patterns, and the result is shown in Fig. 3.9. From the simulation results, it is quite obvious that both Bayer-ordered dithering and error-diffusion dithering can well represent a sinusoidal pattern and have significantly smaller phase errors even with wide fringe periods. This demonstrates a great improvement in the binary defocusing technique. In addition, as indicated in the phase errors, error-diffusion dithering has higher accuracy than Bayer-ordered dithering.

However, binary dithering techniques also have their limitations. A simulation was performed when the dithered pattern was nearly focused (emulated by Gaussian smoothing with a small filter size of 3×3), and the result is shown in Fig. 3.10. Here, we can see that neither the Bayer-ordered dithering pattern nor the error-diffusion dithering pattern could well approximate a sinusoidal pattern when not sufficiently defocused, as shown in Fig. 3.10(c) and Fig. 3.10(g). Moreover, the phase error is quite large, as shown in Fig. 3.10(d) and Fig. 3.10(h), which will impede the accuracy in real measurement. This limitation could be explained by the working principle of the binary dithering techniques. Since these techniques simply apply a matrix to the whole image, they are not fully op-

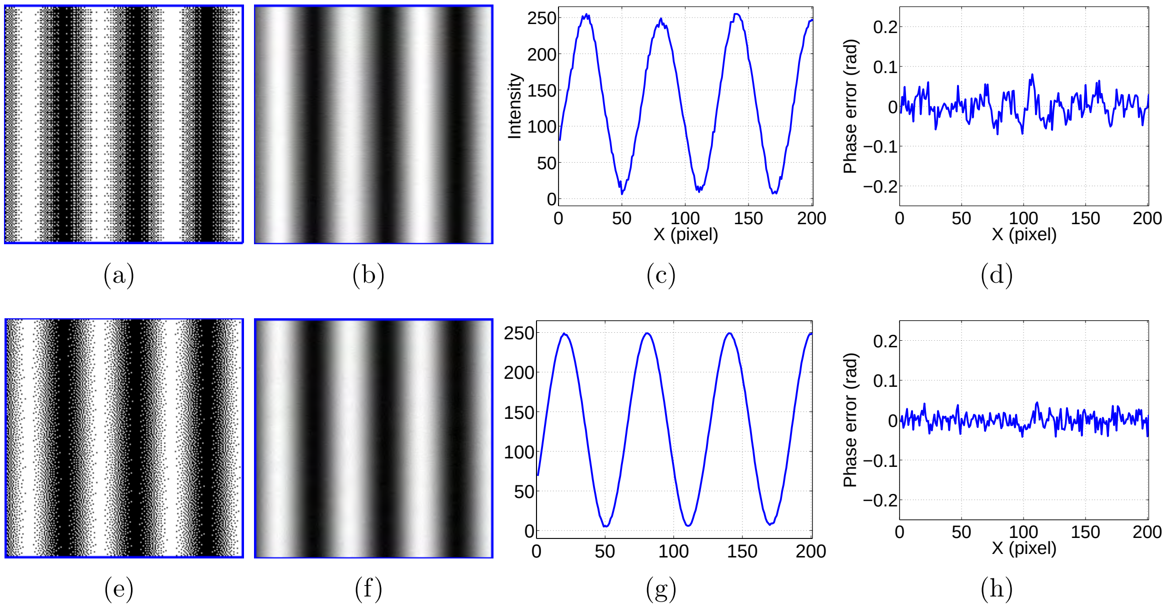

Figure 3.9 Simulation of dithered patterns using a wide fringe period ($T = 60$ pixels). (a) Original Bayer-ordered dithering pattern; (b) the resultant pattern of (a) after Gaussian smoothing with filter-size of 13×13; (c) cross section of (b); (d) cross section of the phase error using pattern (a) with rms error of 0.037 rad; (e) original error-diffusion dithering pattern; (f) the resultant pattern of (e) after Gaussian smoothing with filter-size of 13×13; (g) cross section of (f); (h) cross section of the phase error using pattern (e) with rms error of 0.021 rad.

timized and still leave great room for improvement. Therefore, certain efforts could be made to optimize the binary dithered patterns in order to overcome this limitation.

3.4 Summary

In this chapter, we have introduced the basic principle of the binary defocusing technique and meanwhile illustrated the limitations of the square binary method: (1) Having a projector that is either too focused or too defocused will case a deterioration in the fringe quality and the measurement accuracy, and (2) it does not work well for wide fringe stripes. Then, we introduced the binary dithering techniques that can greatly enhance the performance of the square binary method. However, the residual error is not negligible when the pattern is nearly focused. The binary dithering techniques simply apply

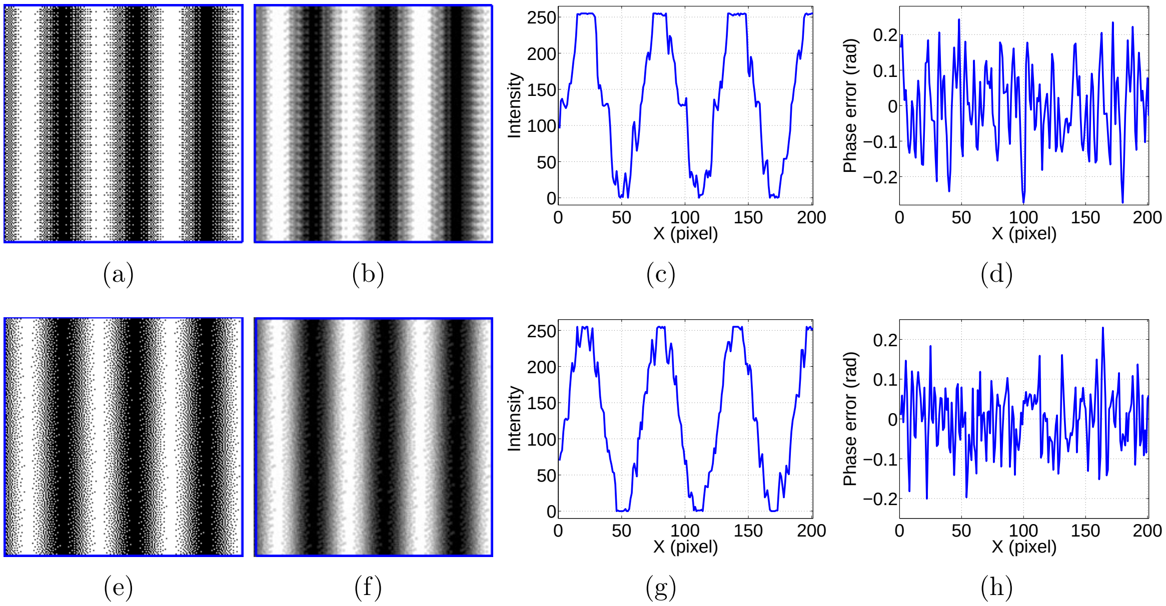

Figure 3.10 Simulation of nearly focused dithered patterns using wide fringe patterns ($T = 60$ pixels). (a) Original pattern; (b) the resultant pattern of (a) after Gaussian smoothing with filter-size of 3 × 3; (c) cross section of (b); (d) cross section of the phase error with rms error of 0.100 rad; (e) original error-diffusion dithering pattern; (f) the resultant pattern of (e) after Gaussian smoothing with filter-size of 3 × 3; (g) cross section of (f); (h) cross section of the phase error using pattern (e) with rms error of 0.075 rad.

matrices to the whole image; therefore, it is possible to come up with some optimization strategies that could improve the performance of the binary dithering techniques. In the next chapter, we will introduce our optimization frameworks that could drastically enhance the performance of the binary dithering technique.

CHAPTER 4. INTENSITY-OPTIMIZED DITHERING APPROACH

In the previous chapter, it is illustrated that the binary dithering technique still has some limitations especially when the pattern is nearly focused, which mainly results from the fact that the binary dithering technique simply applies matrices to the whole sinusoidal pattern. To address the limitations of binary dithering technique, an intensity-optimized dithering approach is proposed in this research, which optimizes the binary dithering pattern in the intensity domain. This chapter presents the local optimization and the global optimization that we developed for this research. Part of this chapter was originally published in *Optics and Lasers in Engineering* (Dai et al., 2014b,a).

4.1 Global Intensity-Optimized Dithering

The binary dithering technique can generate higher quality fringe patterns than the squared binary patterns after projector defocusing. However, it is far from optimal since the dithering techniques essentially apply a matrix to the whole image and do not take full advantages of the sinusoidal structures of the desired sinusoidal fringe patterns. Recently, Dai and Zhang (2013) proposed a phase-based optimization framework to optimize the Bayer-dithering technique when the projector is nearly focused. This method performs optimization in the phase domain by iteratively mutating the status (0 or 1) of a binary pixel. It is demonstrated that for both narrow and wide fringe stripes, substantial improvements could be achieved. However, our further study found that this method was not very stable for different amounts of defocusing. In this section, we will introduce our proposed intensity-based global optimization method to further improve the dithering technique. We will also thoroughly compare the phase-based optimization method with the intensity-based optimization method. Since a 3D shape measurement system utilizes digital fringe projection techniques, the phase quality ultimately determines the measurement quality and thus these two methods are compared in the phase domain. Both simulations and experiments find that the phase-based optimization method is more sensitive to the amount of defocusing, and the intensity-based optimization method can consistently generate high-quality phase with various amounts of defocusing.

4.1.1 Methodology

The main framework of this proposed method can be described by the following steps:

- *Step 1: Error Pixels Detection.* Specifically, taking the difference between the ideal sinusoidal pattern and the Gaussian smoothed binary pattern provides the difference map, from which the error pixels are located. Here, an error pixel refers to the pixel that has intensity error above a given threshold.

- *Step 2: Error Pixel Mutation.* The error pixels are mutated to their opposite status (1s are changed to 0s and 0s are changed to 1s) . After mutations, only good mutations are kept. The good mutation means that the intensity root-mean-square (rms) error between the ideal sinusoidal and the Gaussian smoothed pattern is reduced. If the rms error becomes larger, the original pixel status remains.

- *Step 3: Iteration.* This whole algorithm needs to be performed iteratively since if one of the pixels is altered, its neighboring pixels would also be affected after Gaussian smoothing. Therefore, after getting the whole pattern, it would go back to the previous step until the algorithm converges. The convergence rule we proposed to use is that the improvement of intensity rms errors for a round of processing is less than 0.01%.

- *Step 4: Threshold Reduction.* The threshold is reduced to a smaller number and the whole algorithm goes back to Step 1. The whole algorithm stops when the intensity rms error stabilizes after a number of rounds of iterations. We found that it converges very quickly (typically approximately 15 rounds of iterations).
- *Step 5: Phase Quality Evaluation.* The three-step phase-shifting algorithm introduced in Subsec. 2.2.1 is used to extract the phase and compare with the ideal phase to evaluate the effectiveness of the proposed algorithm.

4.1.2 Global phase-optimized dithering

The phase-based optimization algorithm proposed by Dai and Zhang has also demonstrated its success of improving the dithering technique overall under a certain condition (Dai and Zhang, 2013). The major framework of the phase-based optimization method is almost the same compared with the intensity-based optimization method presented in Subsec. 4.1.1. The main difference between these two methods is that the phase-based method optimizes the dithering technique in the phase domain while the intensity-based method optimizes in the intensity domain. In other words, the rms error used in Steps 1-3 of the intensity-based method is now computed in the phase domain.

Figure 4.1 shows example patterns before and after applying the optimization algorithms. Fig. 4.1(a) shows the desired sinusoidal pattern with a fringe pitch, number of pixels per fringe period, of $T = 18$ pixels. The Bayer-dithering technique with a kernel size of 8×8 will result in the pattern shown in Fig. 4.1(b). We then optimized the pattern with the intensity-based algorithm and the phase-based algorithm, Fig. 4.1(c) and 4.1(d) respectively shows the result.

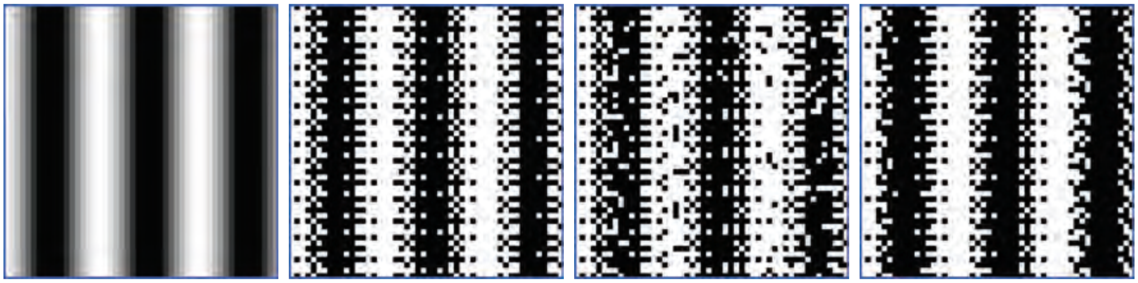
(a) (b) (c) (d)

Figure 4.1 Example of binary patterns after applying different algorithms. (a) Ideal sinusoidal pattern (T = 18 pixels); (b) Bayer-dithered pattern of (a); (c) intensity-based optimized pattern; (d) phase-based optimized pattern.

4.1.3 Simulations

We evaluated the proposed algorithm through simulations where a wide range of fringe stripe breadths were used to ensure that these algorithms could perform well for different practical applications where different density of fringe pattern could be desired. In this simulation, we used fringe pitches T= 18, 24, ..., 114, 120, pixels. The fringe pattern resolution 800 × 600 to match the projector used in our experiments (will be discussed in Sec. 4.1.4).

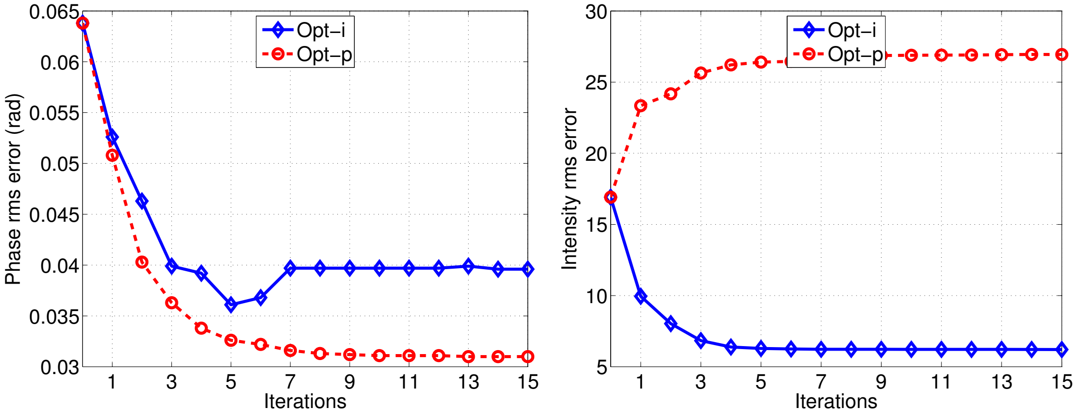

(a) (b)

Figure 4.2 Comparison between the intensity- and phase-based optimization methods for each iteration. The evaluation was performed by applying a Gaussian filter size of 5×5 pixels and standard deviation of 5/3 pixels. (a) Phase rms error; (b) intensity rms error.

Figure 4.2 illustrates the optimization process for a fringe pitch of $T = 18$ pixels. We used a very small Gaussian filter (size: 5×5 pixels and standard deviation $5/3$ pixels) to evaluate the phase rms error after each iteration. The very small Gaussian filter was used to emulate the nearly focused projector. The phase error is determined by comparing against the ideal phase generated by ideal sinusoidal fringe patterns. Figure 4.2(a) shows the results after approximately 15 rounds of iterations with the intensity-based and the phase-based optimization method, where 0 iteration means the starting point where all patterns are the original Bayer-dithered patterns. Compared with the Bayer-dithered patterns, both optimization methods can drastically reduce the phase rms errors. This figure also indicates that after around 10 iterations, both algorithms stabilized. In this research, we used 15 rounds of iterations for all pattern optimizations to ensure the algorithms converge. One may also notice that the phase-based optimization performs better than the intensity-based method for this evaluation condition: Gaussian filter size is 5×5 pixels and standard deviation $5/3$ pixels. Furthermore, one may observe that for the intensity-based optimization method, the phase rms error slightly increases after a number of iterations. This is because the method optimize the patterns in intensity domain before they are evaluated in phase domain. Figure 4.2(b) illustrates the intensity rms errors for each iterations. As expected, for the intensity-based optimization method, the intensity rms error reduces with the increased number of iterations, and then stabilizes. However, for the phase-based optimization method, the intensity differences actually increase after optimization, which is completely unexpected.

We further evaluated the performance of these two types of optimization methods by changing the amounts of defocusing. In simulation, different sizes of Gaussian filters were applied for the optimized patterns under the filter size of 5×5 pixels with the standard deviation of $5/3$ pixels. Figure 4.3 shows the results using three different sizes of Gaussian filters for different optimization algorithms. Under the optimization condition (filter size of 5×5 pixels), Fig. 4.3(a) shows that the phase-based optimization method always

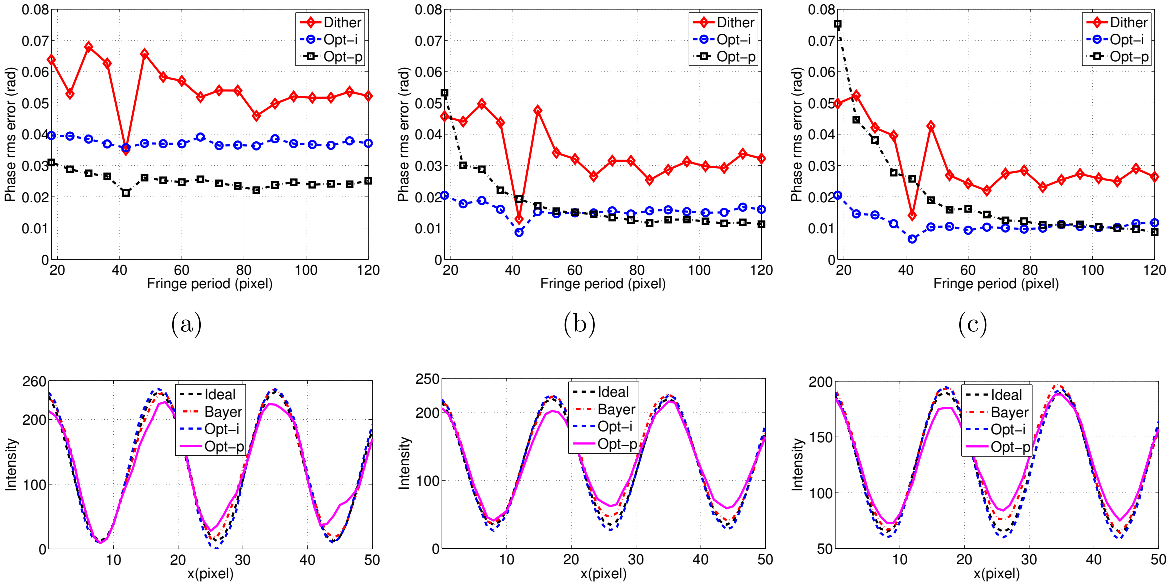

(a) (b) (c)

(d) (e) (f)

Figure 4.3 Performance of the optimized patterns under different amounts of defocusing. (a)-(c) Phase rms errors after applying the 5 × 5, 9 × 9, and 13 × 13 Gaussian filter, respectively; (d)-(f) cross sections after applying the 5 × 5, 9 × 9, and 13 × 13 Gaussian filter, respectively.

performs better than the intensity-based method, which is also indicated by the example shown in Fig. 4.2(a). However, when the filter size was changed to 9 × 9 pixels (standard deviation of 9/3 pixels) or 13 × 13 pixels (standard deviation of 13/3 pixels) meaning that the projector is more defocused, as illustrated in Figs. 4.3(b) and 4.3(c), the performance of the phase-based optimization method, surprisingly, deteriorates rather than improves especially when fringe stripes are narrow (e.g., $T=$ 18 pixels). The performance was even worse than the original Bayer-dithered pattern, making it difficult to understand. On the contrast, the intensity-based optimization method steadily improves with increased filter size, as expected.

To understand the behavior of the phase-based optimization method, Figure 4.3(d)-4.3(f) shows cross sections of the optimized patterns after applying different sizes of Gaussian filters. It can be seen that the phase-based optimized pattern (T = 18 pixels) is not sinusoidal, the larger filter size applied, the large deviation appears to be away from ideal sinusoidal. On the contrast, the intensity-based optimized pattern (again T= 18 pixels) becomes closer and closer to ideal sinusoidal patterns with the increased size of filters. This explains that the phase-based method cannot consistently perform well with different amounts of defocusing.

We believe that the cause of the unstable problem of the phase-based optimization method is that we applied a three-step phase-shifting algorithm to determine the phase. For a three-step phase-shifting algorithm, the intensity does not need to be ideal sinusoidal to obtain ideal phase (Wang and Zhang, 2012). This is because, as indicated in Eq. (2.7), if the intensity of three patterns proportionally change, the phase does not change. This means that a pixel deviates from ideal sinusoidal curve, but it somehow maintains the proportional relationship for three patterns, the phase will be regarded as optimized, and no further mutations should occur.

4.1.4 Experiments

The simulation shows that the intensity-based optimization method has more practical value than the phase-based optimization method in the 3D shape measurement field since the amount of defocusing is difficult to be precisely controlled to the optimization condition. Experiments were also carried out to further evaluate their performance. We utilized a previously developed 3D shape measurement to perform all the experiments. The hardware system includes a digital-light-processing (DLP) projector (Samsung SP-P310MEMX) and a charge-coupled-device (CCD) camera (Jai Pulnix TM-6740CL). The camera was attached with a 16 mm focal length Mega-pixel lens (Computar M1614-MP) with F/1.4 to 16C, and was chosen to have a resolution of 640 × 480 for all experiments. The projector has a native resolution of 800 × 600 with a projection distance of 0.49-2.80 m.

Figure 4.4 shows the phase rms error of measuring a uniform flat white board when the projector is defocused to three different levels using the patterns optimized by the

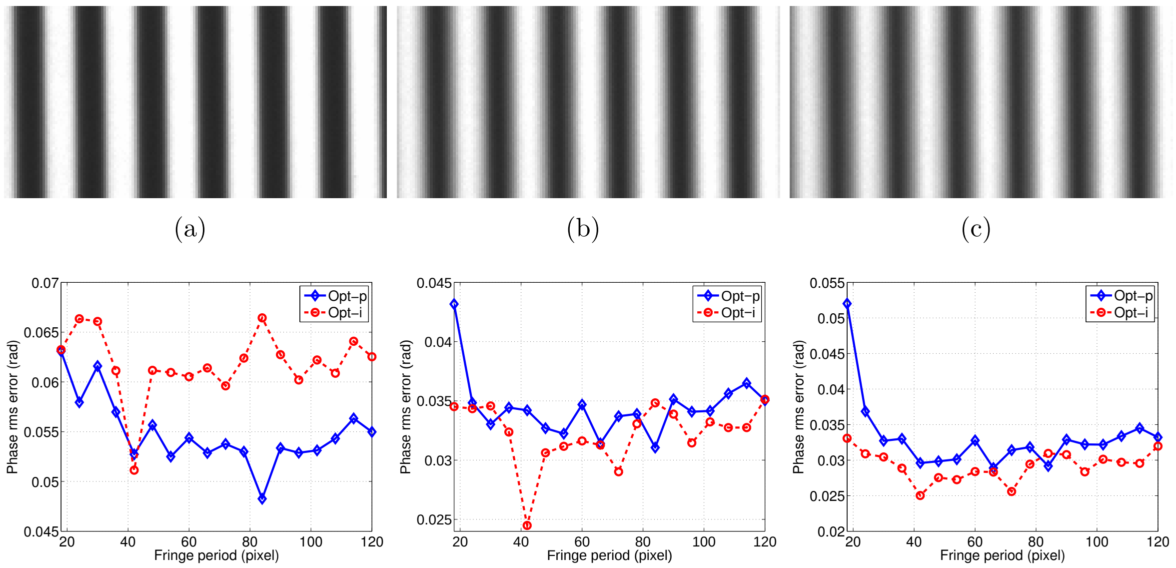

(a) (b) (c)

(d) (e) (f)

Figure 4.4 Experimental results of the optimized patterns under different amounts of defocusing. (a)-(c) Representative squared binary patterns with defocusing level 1 to level 3; (d)-(f) phase rms errors for these three different levels of defocusing using these two optimized fringe patterns with different fringe periods.

phase-based and the intensity-based algorithms. The phase error was computed by taking the difference between the phase obtained from these patterns and the phase obtained by a nine-step phase-shifting algorithm (as introduced in Subsec. 2.2.2 with $N = 9$) with a fringe period of $T = 18$ pixels. Figures 4.4(a)-4.4(c) represent three different levels of defocusing used for a standard squared binary patterns with a fringe period of 18 pixels. The projector starts with being nearly focused to being more defocused. Figures 4.4(d)-4.4(f) show the phase rms errors. This experimental results indicate that when the projector is nearly focused, which is similar to our optimization condition (small amount of defocusing), the phase-based method results in smaller phase rms errors, or better phase quality than the intensity-based method. However, if the projector is more defocused, as shown in Fig. 4.4(e), the intensity-based method starts outperforming the phase-based method in many cases, especially when fringe period is 18 pixels. Furthermore, Figure 4.4(f) shows that if the projector is more defocused, the intensity-based method performs consistently and better than the phase-based method for almost all fringe periods. These experiments further confirm that the intensity-based optimization method indeed can consistently generate high-quality phase while the phase-based method only generate high-quality measurement under a given condition.

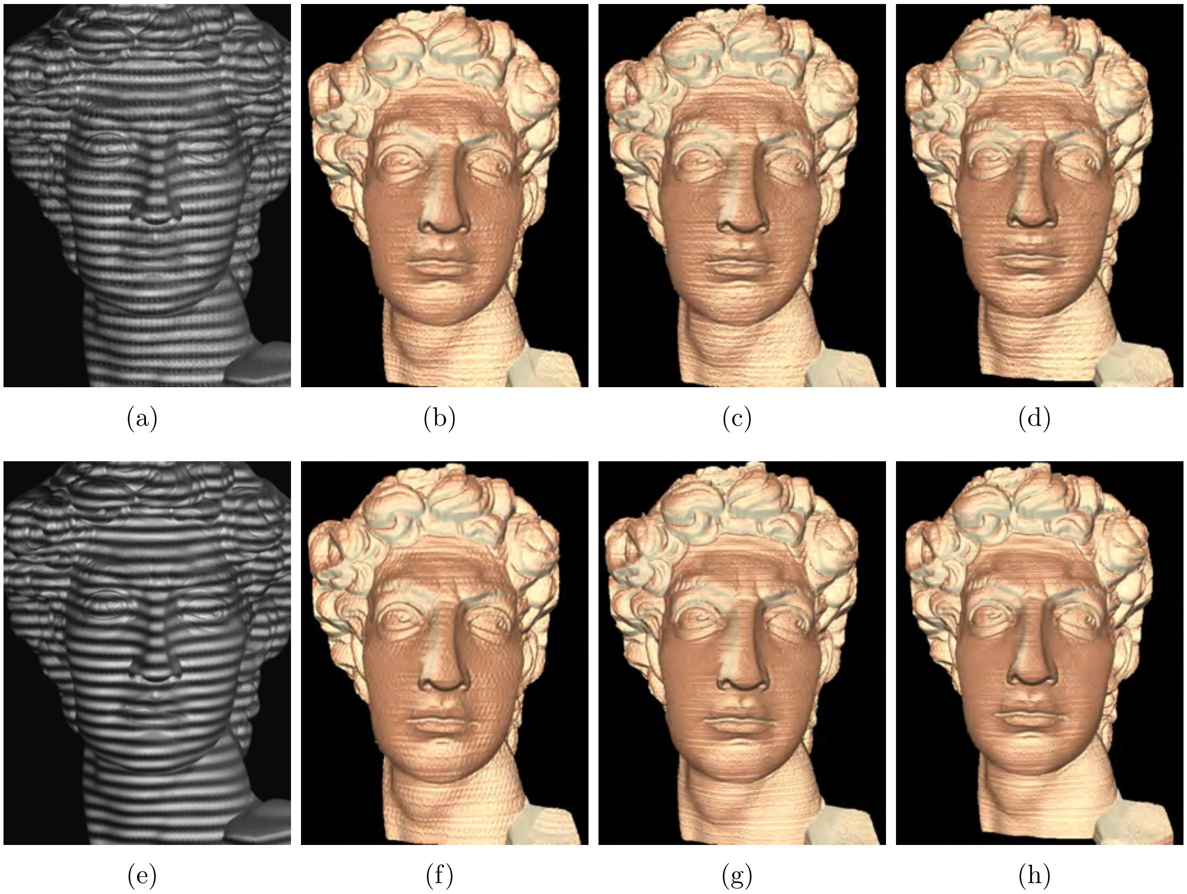
(a) (b) (c) (d)

(e) (f) (g) (h)

Figure 4.5 Measurement results of a complex 3D sculpture. (a) One of the phase-optimized fringe patterns at defocusing level 1; (b)-(d) 3D results using the phase-based optimization method with amount of defocusing level 1 two level 3, respectively; (e) one of the intensity-optimized fringe patterns at defocusing level 1; (f)-(h) 3D results using the intensity-based optimization method with amount of defocusing level 1 two level 3, respectively

We also measured a more complex 3D sculpture to visually compare the differences. Figure 4.5 shows the results and Fig. 4.6 shows the zoom-in views to better visualize the differences. In this experiment, the fringe period we used was $T = 18$ pixels. The absolute phase was obtained by a three-frequency phase-shifting algorithm and the temporal

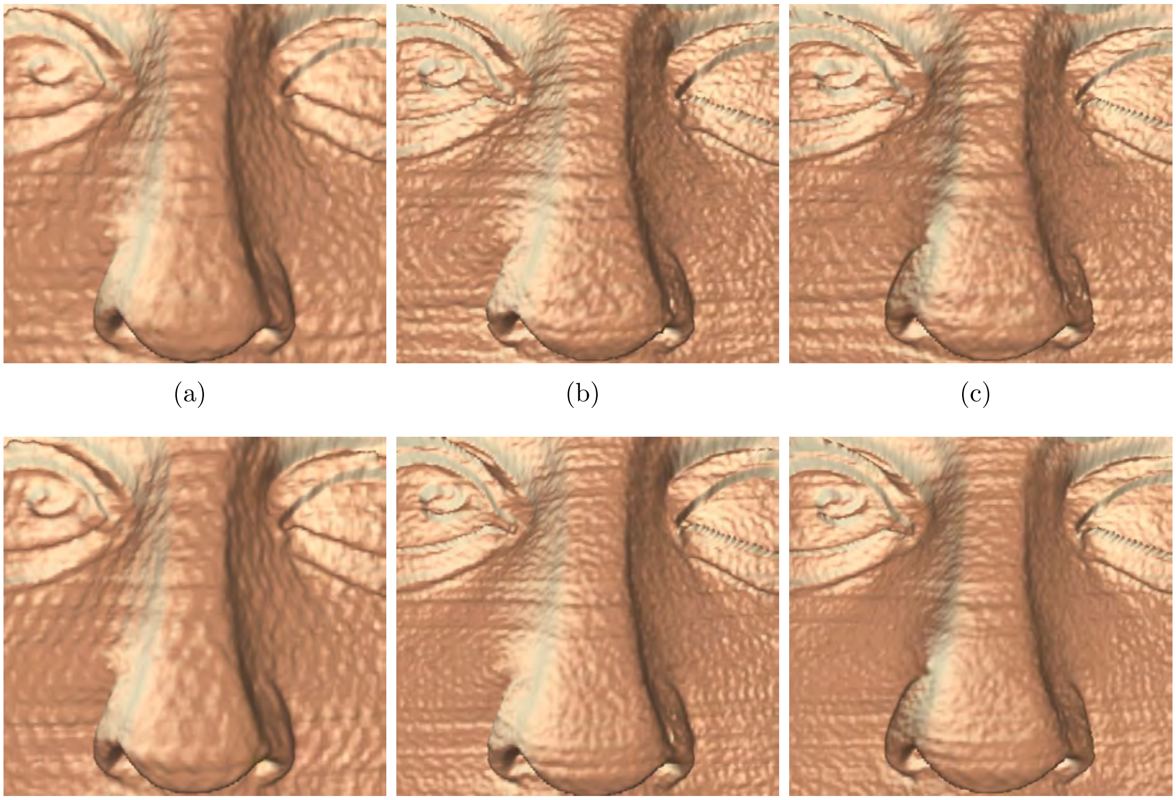

(a) (b) (c)

(d) (e) (f)

Figure 4.6 Close-up view of 3D results shown in Fig. 4.5. (a)-(c) Zoom-in views of the results shown in Fig. 4.5(b)-4.5(d), respectively; (d)-(f) zoom-in views of the results shown in Fig. 4.5(f)-4.5(h), respectively.

phase-unwrapping method whose principle was introduced in Ref. (Wang and Zhang, 2011). The other two fringe periods were 21 and 159 pixels. Figures 4.5(b)-4.5(d) and 4.6(a)-4.6(c) show the increased defocusing amounts for the phase-based optimization method. It appears that the phase-based method did not visually improve the quality of measurement when the amount of defocusing was increased. As a comparison, the results, as illustrated in Figs. 4.5(f)-4.5(h) and 4.6(d)-4.6(f), from the intensity-based optimization patterns are improved when the projector defocusing amount is increased. Even though when the projector is nearly focused, the result from the phase-based optimized method appears slightly better than the intensity-based optimization method, overall, the intensity-based optimization method consistently outperforms the phase-based optimization method.

4.2 Local Intensity-Optimized Dithering

In the previous section, we have illustrated that our global intensity-optimized dithering approach could drastically improve the performance of traditional dithering techniques. However, this global optimization method still has some limitations: (1) since the algorithm is performed globally, it is very time-consuming usually taking quite a long time to converge, and (2) rather than starting with random binary pattern, our optimization algorithm started with traditional dithering patterns and then mutated it based on the difference with ideal sinusoidal patterns which still leaves some room for improvement. The global optimization starting with random binary pattern, however, will be Non-deterministic Polynomial-time (NP) hard, making it impractical to solve the problem mathematically. In this section, we propose a local intensity-optimized dithering method which overcomes the aforementioned limitations. This technique comes from our two observations: (1) the binary patterns should be symmetric for one fringe stripe since the desired sinusoidal patterns are symmetric, and (2) the binary pattern should be periodical in both x and y directions since the desired sinusoidal patterns are periodical in both directions. Based on these two observations, it is practical that we optimize a subset of the image and then generate a whole pattern using symmetry and periodicity. Both simulations and experiments have proven that our local intensity-optimized dithering technique can further enhance the performance of binary dithering technique. It should be noted that instead of comparing the optimization approach with Bayer-ordered dithering as we did for global optimization in Subsec 4.1.3, we compared our local optimization approach with error-diffusion dithering. This is because according to the research results shown in Sec. 3.3, error-diffusion dithering has a better accuracy than Bayer-ordered dithering in measurement results, so here we chose error-diffusion dithering as the control group.

4.2.1 Methodology

Instead of optimizing the desired fringe pattern as a whole (e.g., 800 × 600) as our previously proposed (Lohry and Zhang, 2013; Dai and Zhang, 2013; Dai et al., 2014b), we propose to optimize a subset called *binary patch*, and then tile the patch to generate the full-size patterns using symmetry and periodicity. Unlike those PWM techniques, the proposed technique belongs to area modulation technique where the modulations occur in both x and y directions. Compared with the dithering techniques, the proposed technique strives to generate higher quality fringe patterns with narrow fringe stripes, and similar quality for broad fringe stripes. In addition, unlike the previously proposed method (Lohry and Zhang, 2013; Dai and Zhang, 2013; Dai et al., 2014b) where the optimization is performed under one defocusing level, the proposed method improves fringe quality for different amounts of defocusing.

Assume that the desired sinusoidal fringe patterns vary along x direction: the best-fit binary pattern should be symmetric along x direction for one fringe period (T); and it should be periodic along the y direction. *Row period*, S_y, is defined as the period along y direction. We believe that different breadths of fringe patterns require different optimization strategies, and thus we could utilize different row periods for different breadths of fringe patterns. Instead of directly solving the best-fit NP-hard problem, we propose to modulate a small binary patch for each fringe pattern, and then tile the patch together using symmetry and periodicity of the fringe pattern. The process of modulating a binary patch to generate the whole binary pattern can be divided into the following major steps:

Step 1: Patch Formation. This step initializes the S_y (2 to 10), and defines the number of pixels along x direction. The patch is formed as a dimension of $S_x \times S_y$, here $S_x = T/2$ is one half fringe period.

Step 2: Patch Initialization. Randomly assign each pixel of the $S_x \times S_y$ patch with 0 or 1.

Step 3: Patch Optimization. For each pixel in the binary patch, its binary status is mutated (i.e., 1 to 0 or 0 to 1). If this mutation improves fringe quality, i.e., the intensity root-mean-square (rms) difference between the Gaussian smoothed pattern and the ideal sinusoidal pattern is smaller, the mutation is regarded as a good mutation. It should be noted that mutating one pixel will influence its neighborhood after applying a Gaussian filter. Therefore, the optimization is iteratively performed until the algorithm converges when the rms error difference for a new round of iterations is less than 0.01%.

Step 4: Patch Variation. Repeat Steps 2-3 for a number of times (ranging from 50-500 times) to generate a number of good candidates for each S_y, a number of good patches could be generated because of the random initialization.

Step 5: Patch Dimension Mutation. Change S_y to another value (i.e., 2 to 10), and go to Step 2.

Step 6: Patch Selection. After a number of patch mutations, a set of optimized patches are generated. From these patches, the *best patch* is selected based on the following two rules: (1) phase error does not change drastically if a different size of Gaussian filter is applied; and (2) the resultant phase error is consistently small. These two rules imply that the best patch under one amount of defocusing may not be chosen. This is one of the fundamental difference between our algorithm and the previously developed genetic algorithm (Lohry and Zhang, 2013).

Step 7: Fringe pattern generation. Utilizing the symmetry and periodicity properties of the fringe patterns, the desired size fringe pattern was generated by tiling the best patch together.

Figure 4.7 illustrates how to select the final pattern to use. Figures 4.7(a)-4.7(c) shows three examples of optimized patterns when fringe period $T = 18$. Pattern 1 performs the best when the amounts of defocusing is larger (Gaussian filter size 11 or larger). If one considers the well defocused projector, this might be a good candidate. However, our major focus is to improve the fringe quality when the projector is nearly focused (i.e., Gaussian filter size is small). However, this candidate does not perform well with small amount of defocusing. Therefore, we did not chose this candidate. Pattern 2 depicts the smallest phase error when the filter size is 7 or 11, but does not perform consistently well. This one was not chosen since we require the pattern consistently perform well over different amounts of defocusing. Pattern 3 is the one we chose because this pattern performs consistently across different amounts of defocusing.

From this figure, one may also notice that the phase rms error fluctuates with the increased size of Gaussian filter. This is because our proposed optimization was performed under a special amount of defocusing, i.e., a fixed size of Gaussian filter (5 x 5 in our case). However, because the optimized pattern is the best pattern among those candidates, is not the result of exhaustive search, we cannot guarantee that the phase rms error is still minimized for different amounts of defocusing. Nevertheless, even with such fluctuations, the phase rms error is always smaller than the error-diffusion dithering technique, as will be shown in Fig 4.8 and Fig. 4.9, indicating the success of the proposed method.

4.2.2 Simulations

We simulated different amounts of defocusing by applying different sizes of Gaussian filters. The smallest Gaussian filter was 5×5 with a standard deviation of 5/3 pixels, and the largest was 13×13 with a standard deviation of 13/3 pixels. Gaussian filter size of 5×5 represents the case that the projector is nearly focused, whilst 13×13 represents the case when the projector is defocused to a certain degree. We did not use larger filter sizes as they will jeopardize the fringe contrast, which is not usually used in real measurements. The phase error $\Delta\Phi$ was calculated by taking the difference between the phase obtained from the smoothed binary patterns, Φ^b, and the phase obtained from the

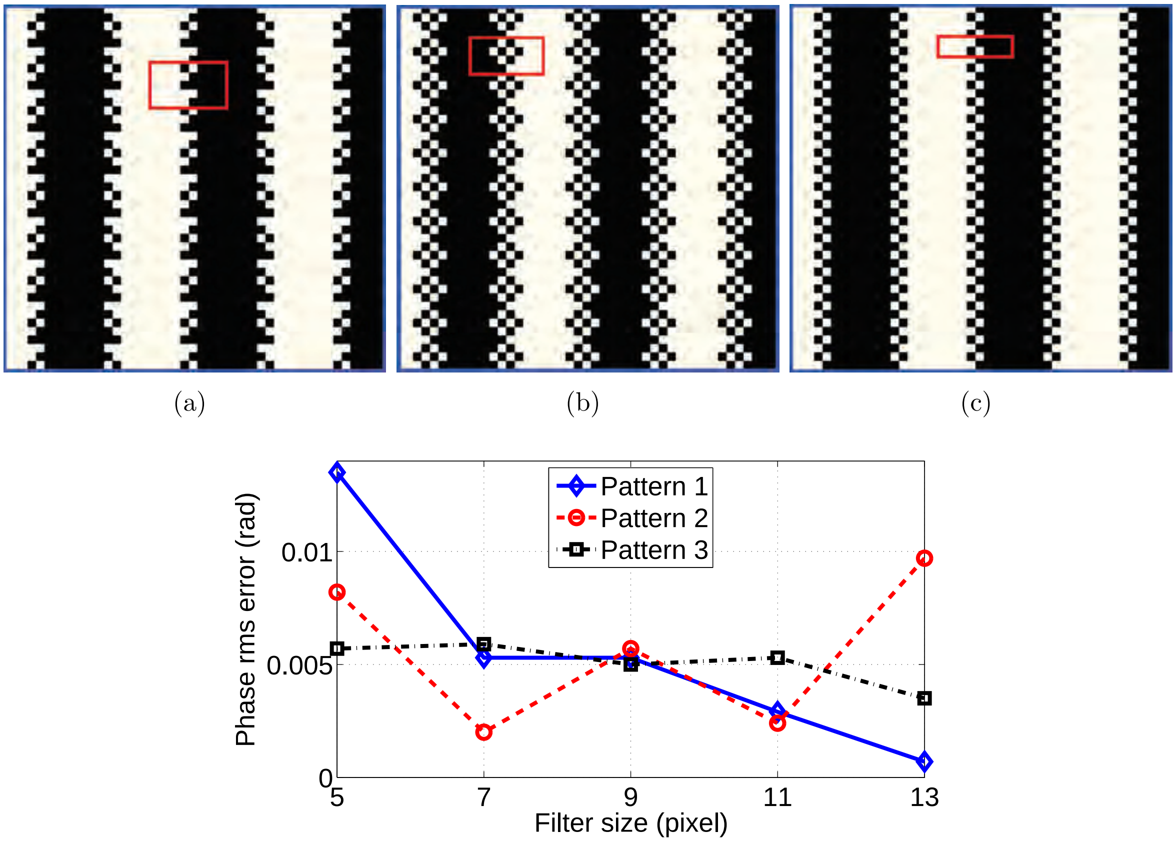

(a) (b) (c)

(d)

Figure 4.7 Example of selecting the pattern from the optimized binary patches. (a) Pattern 1: $T = 18$, $S_y = 5$; (b) pattern 2: $T = 18$, $S_y = 4$; (c) pattern 3: $T = 18$, $S_y = 2$; (d) phase rms error with different amounts of defocusing.

ideal sinusoidal fringe patterns, Φ^i. $\Delta\Phi_o = \Phi_o^b - \Phi^i$ is the phase error obtained from the optimized binary patterns, and $\Delta\Phi_e = \Phi_e^b - \Phi^i$ is the phase error using the error-diffusion dithered patterns.

Figure 4.8 shows the simulation results. The simulation results clearly show that the proposed method can substantially improve the fringe quality for different amounts of defocusing. For instance, the improvement is over 40% when fringe period $T = 18$ pixels. It also indicates that when the fringe period increases, the improvement decreases. This is because the error-diffusion technique has already generated good quality sinusoidals for low-frequency patterns.

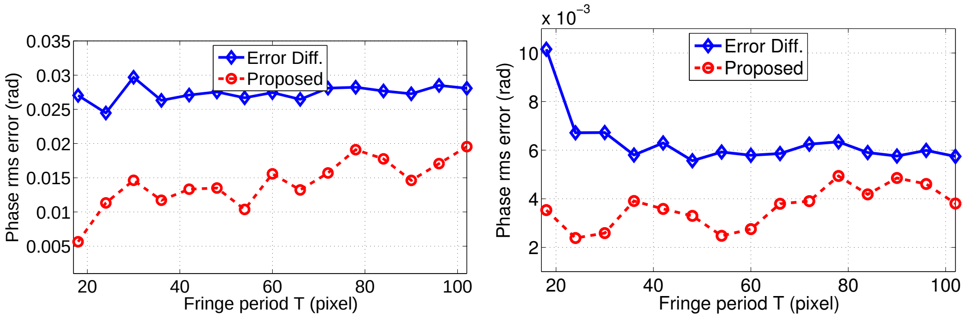

(a) (b)

Figure 4.8 Comparing the phase quality between the proposed method and the Floyd-Steinberg error-diffusion technique. (a) Gaussian filter size of 5 × 5 pixels and standard deviation of 5/3 pixels; (b) Gaussian filter size of 13 × 13 pixels and standard deviation of 13/3 pixels.

4.2.3 Experiments

We also conducted experiments to verify the performance of the proposed technique. The 3D shape measurement system includes a digital-light-processing (DLP) projector (Samsung SP-P310MEMX) and a charge-coupled-device (CCD) camera (Jai Pulnix TM-6740CL). The camera is attached with a 16 mm focal length Mega-pixel lens (Computar M1614-MP) with F/1.4 to 16C. The camera has a resolution of 640 × 480, and the projector has a native resolution of 800 × 600 with a projection distance of 0.49–2.80 m.

We experimentally verified the simulation results by measuring a flat white board using all these fringe patterns. Figure 4.9 shows the results. The phase errors were determined by taking the difference between the phase obtained from the binary patterns (the dithered patterns and the proposed patterns) after Gaussian smoothing and the phase obtained from the ideal sinusoidal patterns. Again, the proposed algorithm generated better results than the error-diffusion algorithm at different amounts of defocusing.

A more complex 3D statue was measured to visually compare these methods. Figure 4.10 shows the results. Figure 4.10(a) shows one of the binary patterns, indicating that the projector was nearly focused. In this experiment, we used the fringe period of $T = 18$ pixels, and converted the phase to depth using the simple reference-plane based

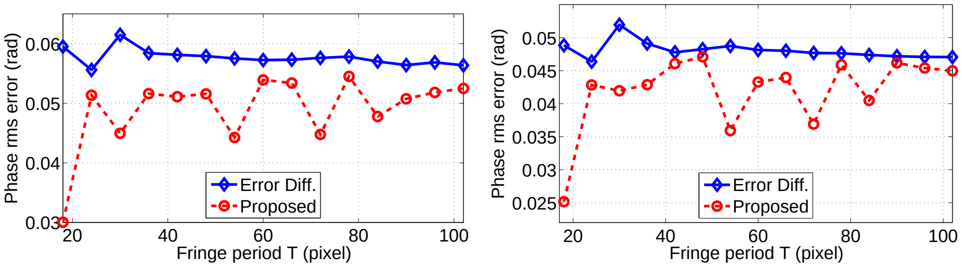

(a) (b)

Figure 4.9 Experimentally comparing the phase quality between the proposed method and the Floyd-Steinberg error-diffusion technique. (a) Nearly focused; (b) slightly defocused.

method discussed in Ref. (Xu et al., 2011). This figure shows that at different amounts of defocusing, the results obtained by using the proposed method are much better than the error-diffusion method, or the squared binary technique.

Figure 4.11 shows the zoom-in views around the nose areas for the measurement results. These results clearly show that when the projector is nearly focused, neither the squared binary method nor the dithering technique could provide reasonable quality measurement; and the proposed technique could perform much better than both methods. When projector is slightly defocused, all these techniques can perform well with the proposed method yielding the best result, again. It is interesting to notice that when the projector is nearly focused, the standard error-diffusion dithering technique actually cannot outperform the squared binary method. This is because the error-diffusion technique tries to keep low frequency information while sacrifices high frequency information, and the fringe frequency here is quite high for fringe period of 18 pixels.

4.3 Discussions And Conclusions

4.3.1 Global optimization

Global intensity-based optimization can essentially improve the performance of Bayer-ordered dithering technique. Moreover, compared with the phase-based optimization

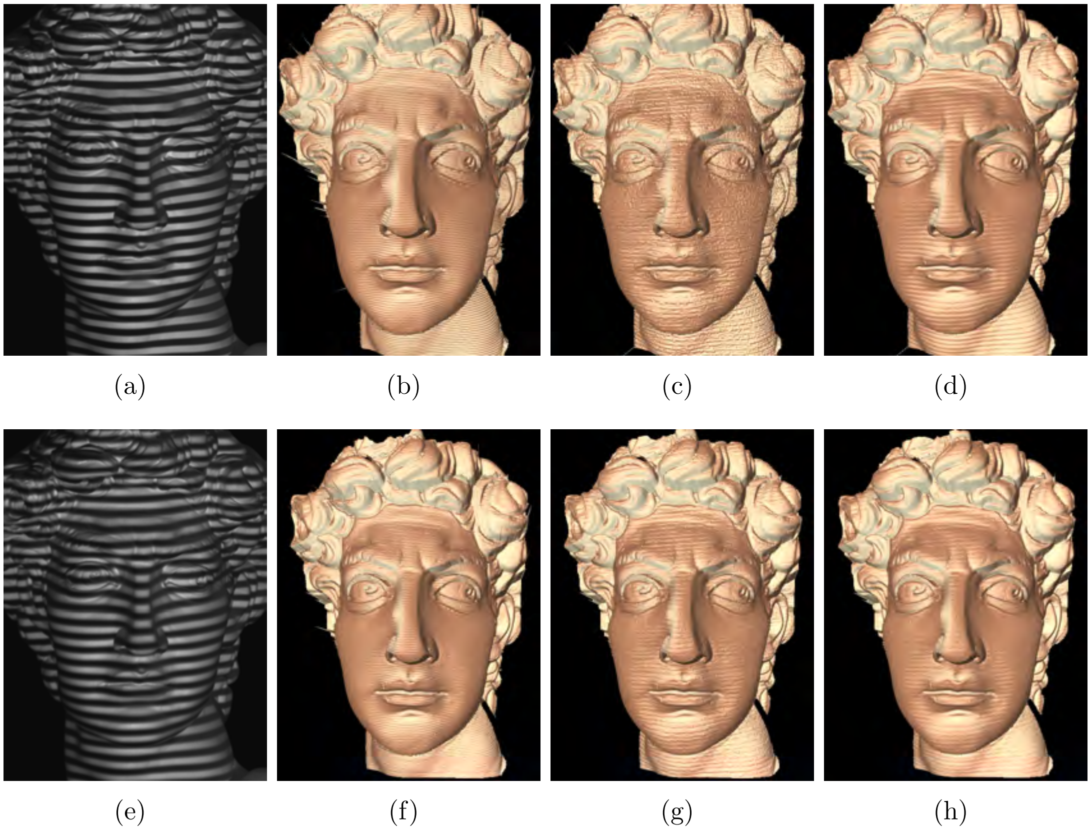

Figure 4.10 Measurement results of a complex 3D statue. (a) One nearly focused fringe pattern; (b)-(d) respectively shows the 3D result with squared binary pattern, the dithered patterns, and the proposed patterns when the projector is nearly focused; (e) one slightly defocused fringe pattern; (f)-(h) respective shows the 3D result with the squared binary pattern, the dithered patterns, and the proposed patterns when the projector is slightly defocused.

method, this intensity-based method can more consistently generate high-quality phase under different amounts of defocusing, while the phase-based optimization method can perform better only under a certain condition, especially when fringe stripes are narrow. From our simulation and experimental results, it seems that intensity-based optimization method has more practical value than the phase-based optimization method. This is because it is very difficult to precisely control the measurement condition to match with the optimal condition requirements of the phase-based method.

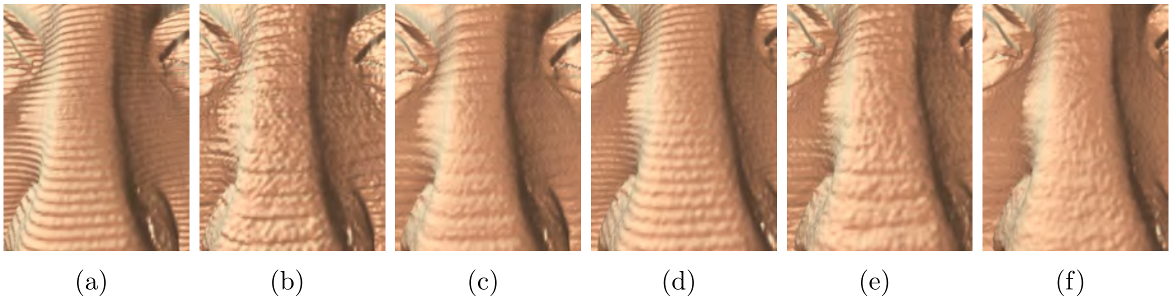

Figure 4.11 Zoom-in views around the nose areas for measurement results with different methods. (a)-(c) respectively shows the zoom-in view of the results shown in Fig. 4.10(b)-4.10(d) when the fringe is nearly focused; (d)-(f) respectively shows the zoom-in view of the results shown in Fig. 4.10(b)-4.10(d) when the projector is slightly defocused.

4.3.2 Local optimization

Local intensity-based optimization, as shown both in simulations and experiments, can drastically improve a more advanced error-diffusion dithering for different amounts of defocusing. For local intensity-based optimization framework, it inherently adopted genetic algorithm for pattern evolution and optimization. Compared with the genetic optimization algorithm proposed previously (Lohry and Zhang, 2013) which did a global optimization toward the image, the proposed method has the merit of speed (seconds instead of hours). It also has the advantage of generating periodical patterns, making it easier to be realized on hardware since the element used is very small. In addition, the proposed algorithm can ensure high-quality phase for different amounts of defocusing while the genetic algorithm cannot.

Compared with all previous research along the same direction (Lohry and Zhang, 2013; Wang and Zhang, 2002; Dai and Zhang, 2013), this proposed method is fundamentally different from any of them, where they either directly generated binary patterns using a dithering technique (Wang and Zhang, 2002), or modified the dithered patterns through some optimization strategies (Lohry and Zhang, 2013; Dai and Zhang, 2013). In other words, they all started from the dithered patterns. The proposed technique, in contrast, starts with randomly assigned patterns, and performs optimization.

However, the proposed algorithm does involve some manual process when two candidates generates similar results. For example, for fringe period $T = 24$, we have two candidate patches shown in Fig. 4.12. Pattern 1 was chosen because the phase error performs more consistently across different amounts of defocusing, as shown in Fig. 4.12(c). One may notice that Pattern 1 actually has larger phase error when filter size is 9 × 9 than Pattern 2.

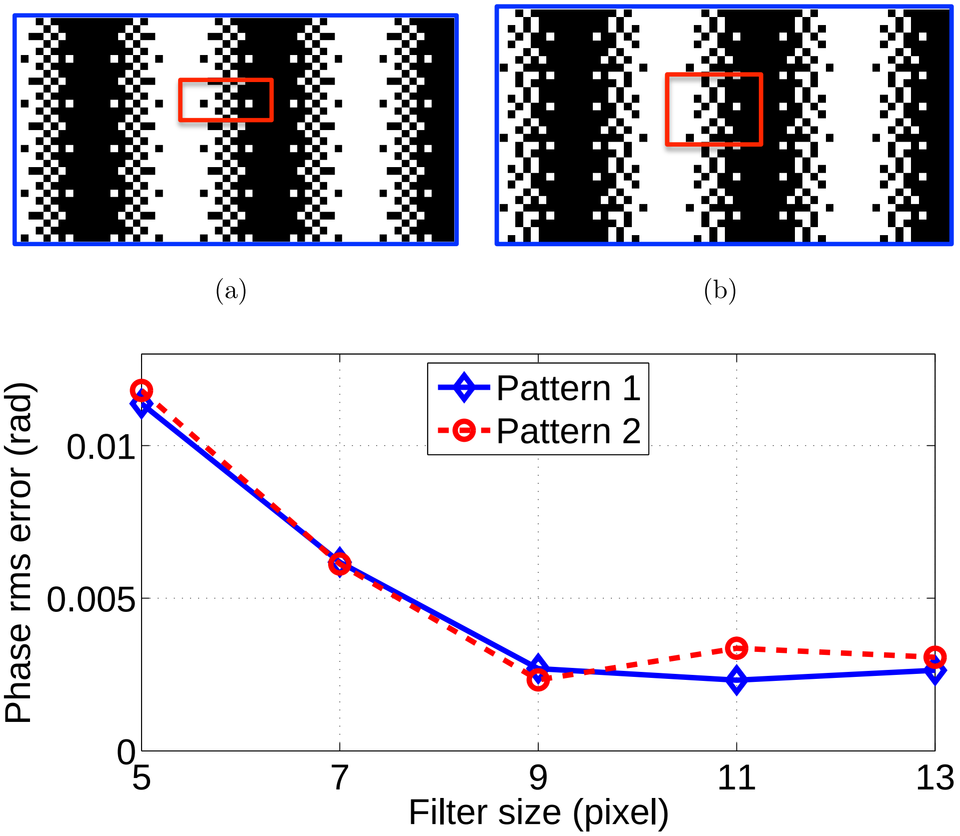

(a) (b)

(c)

Figure 4.12 Example of selecting the pattern from the optimized binary patches. (a) Pattern 1: $T = 24$, $S_y = 6$; (b) pattern 2: $T = 24$, $S_y = 9$; (c) phase rms error with different amounts of defocusing.

4.4 Summary

In this chapter, we presented our global and local intensity-optimized dithering approaches. The global optimization strategy drastically improves the performance of Bayer-ordered dithering over different fringe periods. Moreover, compared with phase-based optimization, it has a more consistent performance over different amounts of defocusing. The local optimization strategy can enhance the performance of a more advanced error-diffusion dithering and save the computational time of the global algorithm. Both simulations and experiments have verified the success of our proposed approaches.

CHAPTER 5. SUMMARY AND FUTURE WORK

This chapter summarizes the contribution of this dissertation research and provides some perspectives about possible future research.

5.1 Research Achievements

In this research, we presented two new intensity-optimized dithering approaches that further optimized the binary dithering technique for high-quality 3D shape measurement. The efforts were first made to optimize the dithered pattern globally based on its difference with the intensities of ideal sinusoidal patterns. Our global optimization framework can substantially improve the performance of the Bayer-ordered dithering technique by 25% overall and up to 50% for the small fringe period (e.g. $T = 18$ pixels). Moreover, compared with previous optimization frameworks, our optimization framework is able to provide consistent accuracy over different amounts of defocusing. However, this global optimization method is still not the perfect solution since the algorithm is performed globally; this is usually computational expensive. Therefore, a local optimization method was proposed which only optimizes a small block of the whole image and builds up the whole image based on symmetry and periodicity. The local optimization algorithm, as shown both in simulation and experiments, can improve the performance of a more advanced error-diffusion dithering technique by 20% overall, and up to 40% for the smallest fringe stripe (e.g. $T = 18$ pixels).

On the whole, the local intensity-based optimization is recommended since it enhances the performance of a more accurate error-diffusion dithering technique. Moreover, since the algorithm is performed locally, it greatly saves the amount of time that should be used to generate one set of optimized fringe patterns.

5.2 Future Work

The local optimization framework leaves some room for improvement. We suggest methods to further overcome two major limitations:

- *Algorithm automation.* As discussed in Subsec. 4.3.2, the local optimization algorithm involves some manual selection process between candidate patterns especially when the two candidate patterns provide similar performances. Therefore, in the future, we should seek to make the whole algorithm automatic. In order to realize an automatic search of optimal patterns, global quantified selection criteria is necessary, and efforts should be made to ensure that the selected patterns will perform consistently over different fringe periods and degrees of defocusing.
- *Improving local optimization algorithm.* Since the local optimization algorithm is inherently combined with a genetic algorithm, we did not do exhaustive search on all possible patterns, which means that our selected pattern might not be optimal. Therefore, it could be possible to come up with a more advanced searching strategy that could achieve a higher convergence rate, and meanwhile maintain a consistent accuracy.

BIBLIOGRAPHY

Albarelli, A., Rodolà, E., and Torsello, A. (2009). Robust camera calibration using inaccurate targets. *Trans. Pattern Anal. Mach. Intell*, 31(2):376–383.

Ayubi, G. A., Ayubi, J. A., Martino, J. M. D., and Ferrari, J. A. (2010). Pulse-width modulation in defocused 3-d fringe projection. *Opt. Lett.*, 35:3682–3684.

Bayer, B. (1973). An optimum method for two-level rendition of continuous-tone pictures. *IEEE International Conference on Communications*, 1:11 – 15.

Carrihill, B. and Hummel, R. (1985). Experiments with the intensity ratio depth sensor. *Computer Vision, Graphics, and Image Processing*, 32(3):337–358.

Chazan, G. and Kiryati, N. (1995). *Pyramidal intensity-ratio depth sensor*. Department of Electrical Engineering, Technion Israel Institute of Technology.

Dai, J., Li, B., and Zhang, S. (2013). Improve dithering technique for 3d shape measurement: phase vs intensity optimization. In *Proc. SPIE*, San Diego, California.

Dai, J., Li, B., and Zhang, S. (2014a). High-quality fringe pattern generation using binary pattern optimization through symmetry and periodicity. *Opt. Laser Eng.*, 52:195–200.

Dai, J., Li, B., and Zhang, S. (2014b). Intensity-optimized dithering technique for high-quality 3d shape measurement. *Opt. Laser Eng.*, 53:79–85.

Dai, J. and Zhang, S. (2013). Phase-optimized dithering technique for high-quality 3d shape measurement. *Opt. Laser Eng.*, 51(6):790–795.

Duane, C. B. (1971). Close-range camera calibration. *Photogrammetric engineering*, 37(8):855–866.

Floyd, R. and Steinberg, L. (1976). An adaptive algorithm for spatial gray scale. In *Proc. Society for Information Dispplay*, volume 17, pages 75–77.

Geng, J. (2011). Structured-light 3d surface imaging: a tutorial. *Advances in Opt. and Photonics*, 3(2):128–160.

Ghiglia, D. C. and Pritt, M. D. (1998). *Two-Dimensional Phase Unwrapping: Theory, Algorithms, and Software*. John Wiley and Sons, Inc, New York, NY.

Gong, Y. and Zhang, S. (2010). Ultrafast 3-d shape measurement with an off-the-shelf dlp projector. *Opt. Express*, 18(19):19743–19754.

Hornbeck, L. J. (1997). Digital light processing for high-brightness, high-resolution applications. In *Proc. SPIE*, volume 3013, pages 27–40.

Huang, L., Zhang, Q., and Asundi, A. (2013a). Camera calibration with active phase target: improvement on feature detection and optimization. *Optics letters*, 38(9):1446–1448.

Huang, L., Zhang, Q., and Asundi, A. (2013b). Flexible camera calibration using not-measured imperfect target. *Applied optics*, 52(25):6278–6286.

Huang, P. S., Zhang, S., and Chiang, F.-P. (2005). Trapezoidal phase-shifting method for three-dimensional shape measurement. *Opt. Eng.*, 44(12):123601.

Huang, Y. H., Shang, Y., Liu, Y., and Bao, H. (2013c). 3d shapes from speckle. *Handbook of 3D Machine Vision: Optical Metrology and Imaging*, page 33.

Jia, P., Kofman, J., and English, C. (2007). Multiple-step triangular-pattern phase shifting and the influence of number of steps and pitch on measurement accuracy. *Appl. Opt.*, 46(16):3253–3262.

Karpinsky, N. and Zhang, S. (2012). High-resolution, real-time 3-d imaging with fringe analysis. *Real Time Image Proc.*, 7(1):55–66.

Kite, T. D., Evans, B. L., and Bovik, A. C. (2000). Modeling and quality assessment of halftoning by error diffusion. *IEEE International Conference on Image Processing*, 9(5):909 – 922.

Lavest, J., Viala, M., and Dhome, M. (1998). Do we really need an accurate calibration pattern to achieve a reliable camera calibration? In *Computer Vision ECCV'98*, pages 158–174. Springer.

Lei, S. and Zhang, S. (2009). Flexible 3-d shape measurement using projector defocusing. *Opt. Lett.*, 34(20):3080–3082.

Lei, S. and Zhang, S. (2010). Digital sinusoidal fringe generation: defocusing binary patterns vs focusing sinusoidal patterns. *Opt. Laser Eng.*, 48(5):561–569.

Li, B., Gibson, J., Middendorf, J., Wang, Y., and Zhang, S. (2013). Comparison between lcos projector and dlp projector in generating digital sinusoidal fringe patterns. In *Proc. SPIE*, San Diego, California.

Li, B., Wang, Y., Dai, J., Lohry, W., and Zhang, S. (2014). Some recent advances on superfast 3d shape measurement with digital binary defocusing techniques. *Opt. Laser Eng.*, 54:236–246.

Lohry, W. and Zhang, S. (2012). 3d shape measurement with 2d area modulated binary patterns. *Opt. Laser Eng.*, 50(7):917–921.

Lohry, W. and Zhang, S. (2013). Genetic method to optimize binary dithering technique for high-quality fringe generation. *Opt. Lett.*, 38(4):540–542.

Malacara, D., editor (2007). *Optical Shop Testing*. John Wiley and Sons, New York, NY, 3rd edition.

Posdamer, J. and Altschuler, M. (1982). Surface measurement by space-encoded projected beam systems. *Computer graphics and image processing*, 18(1):1–17.

Purgathofer, W., Tobler, R., and Geiler, M. (1994). Forced random dithering: improved threshold matrices for ordered dithering. *IEEE International Conference on Image Processing*, 2:1032 – 1035.

Schmalz, C., Forster, F., and Angelopoulou, E. (2011). Camera calibration: active versus passive targets. *Optical Engineering*, 50(11):113601–113601.

Schuchman, T. L. (1964). Dither signals and their effect on quantization noise. *IEEE Trans. Communication Technology*, 12(4):162 – 165.

Sobel, I. (1974). On calibrating computer controlled cameras for perceiving 3-d scenes. *Artificial Intelligence*, 5(2):185–198.

Strobl, K. H. and Hirzinger, G. (2011). More accurate pinhole camera calibration with imperfect planar target. In *Computer Vision Workshops (ICCV Workshops), 2011 IEEE International Conference on*, pages 1068–1075. IEEE.

Stucki, P. (1981). Meccaa multiple-error correcting computation algorithm for bilevel hardcopy reproduction. Technical report, IBM Res. Lab., Zurich, Switzerland.

Tsai, R. (1987). A versatile camera calibration technique for high-accuracy 3d machine vision metrology using off-the-shelf tv cameras and lenses. *Robotics and Automation, IEEE Journal of*, 3(4):323–344.

Wang, Y., Laughner, J. I., Efimov, I. R., and Zhang, S. (2013a). 3d absolute shape measurement of live rabbit hearts with a superfast two-frequency phase-shifting technique. *Opt. Express*, 21(5):5822–5632.

Wang, Y., Li, B., and Zhang, S. (2013b). Superfast 3d shape measurement with binary dithering techniques. *Recent advances in topography research*, pages 43–60.

Wang, Y. and Zhang, S. (2002). Three-dimensional shape measurement with binary dithered patterns. *Appl. Opt.*, 51(27):6631–6636.

Wang, Y. and Zhang, S. (2010). Optimum pulse width modulation for sinusoidal fringe generation with projector defocusing. *Opt. Lett.*, 35(24):4121–4123.

Wang, Y. and Zhang, S. (2011). Superfast multifrequency phase-shifting technique with optimal pulse width modulation. *Opt. Express*, 19(6):5143–5148.

Wang, Y. and Zhang, S. (2012). Comparison among square binary, sinusoidal pulse width modulation, and optimal pulse width modulation methods for three-dimensional shape measurement. *Appl. Opt.*, 51(7):861–872.

Xian, T. and Su, X. (2001). Area modulation grating for sinusoidal structure illumination on phase-measuring profilometry. *Appl. Opt.*, 40(8):1201–1206.

Xu, Y., Ekstrand, L., Dai, J., and Zhang, S. (2011). Phase error compensation for three-dimensional shape measurement with projector defocusing. *Appl. Opt.*, 50(17):2572–2581.

Zhang, C., Huang, P. S., and Chiang, F.-P. (2002). Microscopic phase-shifting profilometry based on digital micromirror device technology. *Applied optics*, 41(28):5896–5904.

Zhang, S. (2010). Recent progresses on real-time 3-d shape measurement using digital fringe projection techniques. *Opt. Laser Eng.*, 48(2):149–158.

Zhang, S., van der Weide, D., and Oliver, J. (2010). Superfast phase-shifting method for 3-d shape measurement. *Opt. Express*, 18(9):9684–9689.

Zhang, Z. (2000). A flexible new technique for camera calibration. *IEEE Trans. Pattern Anal. Mach. Intell.*, 22(11):1330–1334.

Zuo, C., Chen, Q., Feng, S., Feng, F., Gu, G., and Sui, X. (2012). Optimized pulse width modulation pattern strategy for three-dimensional profilometry with projector defocusing. *Appl. Opt.*, 15(19):4477–4490.

Zuo, C., Chen, Q., Gu, G., Feng, S., Feng, F., Li, R., and Shen, G. (2013). High-speed three-dimensional shape measurement for dynamic scenes using bi-frequency tripolar pulse-width-modulation fringe projection. *Opt. Laser Eng.*, 51(8).